ORIGINAL RESEARCH ARTICLE

Simulation of the Axial III Plus Plasma Torch and Its Arc Fluctuations

Jyothi Krishna Perambadur[1] · Vincent Rat[1] · Taha Ngadia Niane[2] ·
Christophe Chazelas[1]

Abstract The demand for utilizing the Axial III Plus plasma spray system has prompted the numerical modeling of its arc plasma torch, integral to creating a digital twin of the suspension plasma spray process. The Axial III Plus plasma torch is a highly efficient and reproducible tool with a unique three-torch exit jet arrangement that allows the axial injection of solid/liquid feedstock, not possible with a single cathode/anode–plasma torch setup. In this study, we employ the local thermodynamic equilibrium approximation of the magnetohydrodynamic (MHD) model to simulate plasma flow inside the single gun plasma torch of Axial III, considering electrode–plasma interactions. Describing electric arc dynamics during restrike proves intricate; thus, a restrike model is used relying on cutoff criteria based on a threshold value E_b of the predicted radial electric field at the electric arc fringes. The model successfully replicates typical electric arc behavior and saw-toothed voltage profiles during restrike, notably capturing the characteristics of the Axial III anode's unique and complicated design variations in electric arc motion and its corresponding arc voltage profile. Analysis extends to studying variations in E_b, which directly influence mean electric arc length, arc voltage, and mean arc spot time, potentially impacting energy generation and losses in the torch. These findings provide a valuable foundation for future simulations of this design, especially with swirl gas injection and ternary gas mixtures.

Keywords axial III plus plasma torch · arc plasma torch modeling · LTE · restrike mode

Abbreviations

LTE	Local thermodynamic equilibrium
SPS	Suspension plasma spray
NLTE	Non-local thermodynamic equilibrium
APS	Atmospheric plasma spray
CAD	Computer-aided design
DC	Direct current

List of Symbols

A	Magnetic potential vector (T-m)
A_G	Richardson constant ($Am^{-2}s^{-2}$)
B	Self-induced magnetic field (T)
C_p	Specific heat (J/kg K)
$d_{i-plasma}$	Distance between the plasma–cathode interface and center of the neighboring plasma cell (m)
$d_{i-cathode}$	Distance between the plasma–cathode interface and center of the neighboring cathode cell (m)
$d_{i-anode}$	Distance between the plasma–anode interface and center of the neighboring anode cell (m)

✉ Jyothi Krishna Perambadur
jyothi-krishna.perambadur@unilim.fr;
krish212332@gmail.com

1 IRCER, CNRS UMR 7315, University of Limoges, 87068 Limoges, France

2 SAFRAN TECH, Pôle Matériaux et Procédés, Rue de Jeunes Bois, CS 80112, 78772 Châteaufort, France

Springer

e	Electron charge (C)
E_b	Threshold electric field (V/m)
E	Electric field (V/m)
$E_{r,\text{mean}}$	Mean radial electric field (V/m)
f_ψ	Flux due to advection and convection of ψ
h	Specific enthalpy (J/kg)
$\bar{\bar{I}}$	Identity tensor
J	Electric current density (A/m^2)
J_{emis}	Thermionic emission of electron flux (A/m^2)
J_{ions}	Current flux due to ion flux (A/m^2)
J_{elec}	Calculated electrical current density at the plasma–anode interface (A/m^2)
k_b	Boltzmann constant (J/K)
n	Surface unit normal
p	Pressure (Pa)
Q_{in}	Inlet mass flow rate (kg/s)
Q_J	Joule heating term (J/(m^{3}s))
Q_r	Volumetric radiation loss (J/(m^{3}s))
$Q_{i,\text{diffusion}}$	Diffusion heat flux at the interface (W/(m^2))
$Q_{\text{additional}}$	Other heat fluxes except the $Q_{i,\text{diffusion}}$ (W/(m^2))
$Q_{\text{rad–cathode}}$	Radiation heat flux absorbed at the cathode (W/(m^2))
Q_{anode}	Heat flux due to electron condensation (W/(m^2))
R	Anode nozzle radius (m)
r_e	Arc column radius (m)
S_ψ	Source/depletion of ψ
t	Time (s)
$T_{i,\text{cathode}}$	Cathode temperature at plasma–cathode interface (K)
$T_{i,\text{plasma}}$	Plasma temperature at plasma–cathode interface (K)
T_{cathode}	Neighboring cathode cell temperature next to the plasma–cathode interface (K)
T_{plasma}	Neighboring plasma cell temperature next to the plasma–cathode interface (K)
T_{elec}	Interface temperature of the plasma–anode regions (K)
u	Plasma velocity field (m/s)
U_C	Fall voltage at the cathode (eV)
U_a	Anode fall voltage (eV)
V_f	Imposed initial voltage (V)
ΔV_j	Volume of the cell j (m^3)
ΔW	Reduction in the work function, given by Schottky correction (eV)

Greek Symbols

d_v	Jump amplitude of arc voltage (V)
Γ_{im}	Coefficient of implicit source term used in momentum equation for electrode regions

λ	Thermal conductivity (W/(m-K))
λ_{cathode}	Cathode thermal conductivity (W/(m-K))
λ_{plasma}	Plasma thermal conductivity (W/(m-K))
$\lambda_{i,\text{effective}}$	Effective thermal conductivity of plasma–cathode interface (W/(m^2-K))
μ_0	Magnetic permeability of free space (H/m)
μ	Laminar viscosity of the plasma (Pa-s)
ρ	Density (kg/m^3)
σ	Electrical conductivity (S/m)
σ_{cathode}	Cathode electrical conductivity (S/m)
σ_{plasma}	Plasma electrical conductivity (S/m)
σ_{anode}	Anode electrical conductivity (S/m)
$\bar{\bar{\tau}}$	Shear stress (Pa)
ϕ	Electric potential (V)
$\phi_{i,\text{cathode}}$	Cathode electrical potential at plasma–cathode interface (V)
$\phi_{i,\text{plasma}}$	Plasma electrical potential at plasma–cathode interface (V)
Φ_i	Lowest ionization energy of plasma species present (eV)
Φ_W	Work function of Tungsten with lanthanum oxide dopant (eV)
Φ_A	Anode material work function (eV)
$\phi_{\text{anode,c}}$	Neighboring anode cell electrical potential next to the plasma–cathode interface (V)
$\phi_{\text{plasma,c}}$	Neighboring plasma cell electrical potential next to the plasma–cathode interface (V)
ϕ_{7000K}	Electrical potential at 7000 K isotherm (V)
ϕ_{anode}	Electrical potential at anode surface (V)
ψ	Volumetric conservative quantity

Introduction

Today, suspension plasma spraying (SPS) is still one of the most studied research themes in the field of thermal spraying (Ref 1,2). This interest is explained by the possibilities for technological development that this process should allow (Ref 3): new-generation thermal barriers for aeronautical and industrial gas turbines, environmental barriers, high-performance anti-wear coatings, glaciophobic coatings on wings aircraft and wind turbine blades, antimicrobial coatings, components for solid oxide fuel cells, etc. In parallel, plasma spray torches with design different from the so-called legacy plasma torches (high arc current and low gas flow rates APS (atmospheric plasma spray) torches: 3 MB, 9 MB, F4 and variations of these (Ref 4) have been developed and are now available on the market. They aim at (i) improving the stability of the plasma jet by limiting the movements of the arc root, (ii) limiting the erosion of the electrodes, in particular of the anode, (iii) increasing the length and the specific enthalpy

of the plasma jet, and (iv) increasing the throughputs of the processed materials. Among these new designs, cascaded anodes plasma torches [e.g., Oerlikon Triplex Pro-210 and Sinplex ProTM and C + APS from TSD Inc, USA] or the Axial III Plus plasma torches from Northwest Mettech Corp are used today for suspension plasma spraying processing of materials.
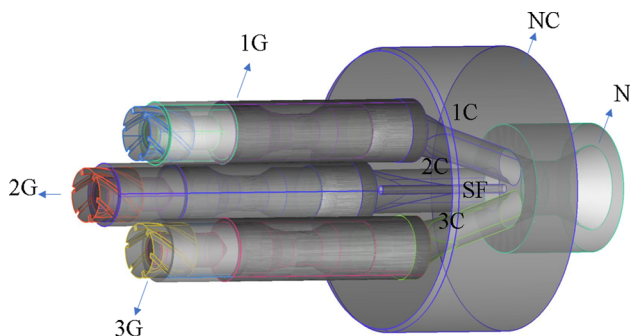
The use for the Axial III Plus plasma torch has been steadily increasing in the suspension plasma spraying market, owing to its distinctive design featuring three individual arc plasma torches, as illustrated in Fig. 1 that displays the CAD view of its design. It illustrates the three torches (1G, 2G, and 3G), powered by three independent direct current (DC) sources, along with their respective converging nozzles (1C, 2C, and 3C), mounted inside a chamber (NC). The converging nozzles (1C, 2C, and 3C) lead into a single wider nozzle (N). To inject the suspension particles, a smaller nozzle (SF) is introduced between the three converging nozzles, and its injection location coincides with the exits of the converging nozzles (1C, 2C, and 3C). This design enables axial feeding of the suspension at the central point of its three converging plasma jets. The advantage of axial feeding, particularly with this configuration, allows for the trapping of particles in the core of the high-temperature jets, ensuring a more uniform treatment of particles and a higher deposition efficiency (up to 80%) than those of the arc plasma torches using radial injection (Ref 5, 6). Moreover, the use of three identical smaller torches in the Axial III setup, rather than a single cathode/anode torch setup with a large processing volume (e.g., other APS torches: 3 MB, 9 MB, F4 (Ref 7)), allows for the use of wider gas compositions and higher mass flow rates, ultimately leading to significantly improved coating efficiencies (Ref 4, 8). Additionally, the Axial III Plus setup offers the advantage of enhancing the lifespan of electrodes by maintaining lower operating currents per torch while keeping the overall electric power high and constant (Ref 5, 9). It is noteworthy that electrode erosion is directly proportional to the square of the operating current applied; therefore, operating at lower arc currents

contributes to prolonging the lifetime of the electrodes. Due to its specific design, Axial III Plus plasma torch can operate over wider operating parameters than the single torch design (i.e., 3 MB, 9 MB, F4): it can be fed with Ar-N_2-He or Ar-N_2-H_2 gas mixtures with a total plasma gas flow rate between 100 and 300 slpm, total arc current intensity between 300 and 750 A (100-250 A per torch), and an electric power level up to 140 kW (Ref 4, 10, 11).

Some experimental works (Ref 6, 9, 12, 13) have focused on the influence of the Axial III Plus torch operating parameters onto plasma jet properties at the torch outlet and coating characteristics; however, the complexity of the process requires numerous tests to produce a coating with controlled properties on a part of complex shape, which slows down its adaptation by manufacturers. Thus, there is a growing interest among researchers and industrial experts in creating a digital twin of the whole process, as part of establishing Industry 4.0. The digital twin of this process will be quite handy in selecting the most appropriate parameters, such as arc current, gas mass flow rate, electrode materials, suspension materials, and its feeding rate. It should therefore make it possible to limit the time, materials, and personnel necessary to develop innovative products more quickly. Therefore, as part of creating the digital twin of the SPS process, the simulation of arc plasma torches is crucial, requiring comprehensive numerical modeling of the arc plasma torch.

Numerical modeling of the arc plasma torch is not entirely new (Ref 14, 15), and significant advances have been made thus far. For instance, there are models based on local thermodynamic equilibrium (LTE) (Ref 16-18), non-equilibrium models (NLTE) (Ref 19-21), and the models that also include electrodes and their coupling (Ref 22, 23), with a few incorporating electrode sheaths. Among these, non-equilibrium modeling with electrode coupling and sheath has seen notable progress, recently being applied to the SinplexPro^{TM} plasma torch, which utilizes a cascaded type of anode—a departure from the lengthier anode accommodated by the Axial III Plus (Ref 24).

The use of non-equilibrium modeling is particularly important for the arc torches in Axial III Plus because these torches operate with lower arc currents (< 200 A) and higher gas flow rates (> 100 slpm) compared to other APS torches (i.e., 3 MB, 9 MB, F4). These operating parameters enhance the thermal disequilibrium near the electrodes and in the cold boundary layer surrounding the arc column. However, the applicability of this model is limited by the availability of thermodynamic and transport properties for the pure gases or gas mixtures under non-equilibrium conditions. Calculating these properties is challenging, especially for mixtures of argon, hydrogen, and nitrogen with varying compositions, and is beyond the scope of this study (Ref 25-28). Therefore, as a preliminary approach, an

Fig. 1 Axial III plus plasma torch cad view

LTE model has been used to simulate a single gun of Axial III Plus with an Ar-H$_2$ mixture. It should be noted that, to the best of the authors' knowledge, non-equilibrium modeling studies have only been conducted for pure argon scenarios due to the limitations in mixture property data (Ref 19, 20, 23, 28, 29).

Another challenging problem in arc plasma torch modeling is simulating the motion of the electric arc during the so-called restrike mode of operation. The restrike mode of plasma torch operation came to light when Pfender and their colleagues investigated to uncover the reasons behind the periodic saw-toothed nature of voltage drop in the plasma torch over time (Ref 31, 32). They discovered that this phenomenon results from the movement of the anode arc attachment downstream and its subsequent arc breakdown, forming a new anode attachment in the upstream direction. This observation became possible due to a specially designed arc tunnel facility that allows the visualization of the electric arc using a transparent window on a part of the anode surface. They further added that the movement of the anode attachment in the downstream direction was mainly associated with an imbalance between fluid dynamic drag and electromagnetic forces at the anode attachment location. As a result, it gradually stretches the arc column length and increases the torch voltage. Subsequently, due to arc breakdown in the upstream direction, a new anode attachment forms, rapidly reducing the arc column length and causing a rapid drop in arc voltage. For an arc plasma torch, the restrike mode is particularly favored by the use of diatomic plasma gases, high gas flow rates and low arc currents during torch operation. As the reattachment process in the restrike mode occurs involving electric fields (10-60 kV/m) that are two orders of magnitude lower than the gas breakdown at atmospheric pressure, the electron avalanche mechanism seems ruled out in the mechanism of breakdown. It was proposed more recently that a thermal instability was put forward as possible mechanism (Ref 33-35).

The breakdown process of the arc column during restrike is not yet quite understood; hence, modeling this process, which involves short time scales, is very complicated within the context of fluid modeling of plasma. Consequently, several simple restrike models can be found in the literature with LTE models. The first of its kind is the model developed by Moreau et al. (Ref 18), which used a mean radial electric field as a parameter determined at the iso-surface of 7000 K. When this value exceeds a certain threshold E_b at a particular location, they introduced a high-temperature radial column with a temperature of 8000 K between that specific location and the anode surface. The main disadvantage of this model is the addition of energy resulting from introducing new columns, which may lead to discrepancies in the overall energy balance.

Another interesting simple model of arc breakdown has been proposed by Trelles et al. (Ref 36), which used the radial instantaneous electric field as a parameter. When the value exceeds a certain threshold E_b at a particular position, instead of introducing a temperature column as done in Moreau et al., a high electric conductivity column with a definite profile has been introduced to create the new attachment column.

In the present work, a LTE model has been applied to simulate one of the arc plasma torches in the Axial III Plus plasma torch using an Ar-H$_2$ mixture. We have applied a restrike model that follows the approach of Moreau et al. (Ref 18) for determining the radial mean electric field at the iso-surface of 7000 K and its location. During the creation of the new arc column to facilitate the new attachment, we have based our approach on the similar method proposed by Trelles et al. (Ref 36), where a constant electrical conductivity column has been introduced. The second section presents the commercial plasma torch geometry, operating conditions used in this study, the numerical model and computational procedure. The third section summarizes and discusses the predictions obtained from the model and focuses (i) the electromagnetic and thermal coupling between the arc and the solid electrodes, (ii) the electric arc dynamic and arc voltage evolution under the restrike mode, and (iii) the plasma jet properties at the torch outlet as well as thermal energy balance of the torch. At last, Section 4 gives the conclusion.

Model Description

In Fig. 2, a detailed inner view of a single gun of the Axial III (one of 1G, 2G, and 3G) is presented, showcasing the cathode (C) and the anode nozzle (A). The cathode is composed of tungsten with a lanthanum oxide dopant at the tip, while the anode nozzle consists of two materials: copper (A1) and pure tungsten (A2). The design of the anode is notably unconventional compared to old legacy APS plasma torch (3 MB, 9 MB and F4), featuring a lengthier copper block with varying diameter (A1)
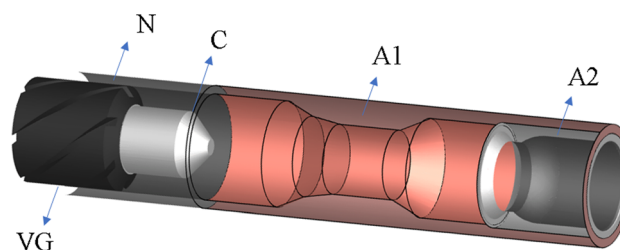
Fig. 2 Internal view of the arc plasma torch used in the Axial III plus setup (N—neutrode, C—cathode, A1—copper anode, A2—tungsten anode)

mounted first, followed by the placement of a pure tungsten block ($\sim$ 1/3rd of A1 length) on top of A1, as illustrated in Fig. 2. The inner lining of the tungsten part of anode nozzle is comprised of tungsten with lanthanum oxide dopant. The space between the cathode and the anode is called the plasma chamber, where plasma formation occurs through electric arc heating. Before starting the torch, cold gas is allowed entering the plasma chamber via a vortex generator (VG). The symbol 'N' represents the wall faces between the inlet and the anode (A1).

The inner surface of the anode in the Axial III Plus torch is notably different from that of anodes used in the legacy APS torches like the 3 MB and 9 MB models. In these torches, the anode nozzle diameter remains relatively constant downstream the cathode tip. However, in the Axial III Plus torch, particularly in the copper region, the anode inner surface features both converging and diverging sections between two wide spacers of the same diameter. These spacers are strategically positioned, with one located after the cathode tip and the other before the start of the tungsten part (A2).

A similar anode design with a varying inner surface has been documented in other research (Ref 8), albeit with slight variations in the structure of the tungsten part. This design is commercialized as the 100HE and is manufactured by Progressive Technology Inc. in Grand Rapids, MI. There are two main differences between the designs of the anode in the 100HE and the single gun of the Axial III: firstly, the wide spacer following the cathode tip is replaced by a longer converging part, and secondly, the design of the A2 tungsten includes individual rings of tungsten mounted on A1. The primary principle behind the design of anode nozzles in both the Axial III gun and the 100HE is to reduce arc fluctuations. The converging section of the anode serves as a potential arc pusher, while the tungsten parts are used to create a stable attachment for the arc and limit anode erosion.

Computational Domain

The computational domain of present study consists of the one of the arc plasma torches (1G, 2G, and 3G) along with its respective nozzle (1C or 2C or 3C). The 3D schematic of this structure can be seen Fig 3(a). This model study is currently aimed to investigate arc dynamic under no swirl component at the inlet, hence the vortex generator (VG) is removed in model geometry. The 2D schematic of computational domain is shown in Fig. 3(b). The computational domain includes four regions namely: (1) plasma region, (2) cathode, (3) anode-C (copper) and (4) anode-T (tungsten). The area of the plasma region is occupied between the inlet ('2'), outlet ('5'), inner surface of the cathode, inner surface of the anode, neutrode surface ('3'), and

converging nozzle surface ('6'). The cathode tip diameter is 1.63 mm. The anode inner diameter varies significantly between 6 and 9 mm. The computational domain is extended to 20 mm length for reducing the influence of boundary effects.

Mathematical Model

The mathematical model solved unsteady Navier–Stokes equations for plasma at non-isothermal conditions along with Maxwell's equations to describe electromagnetic fields in both the plasma and the electrode phases (electrodes). In addition, this model was coupled with transient heat conduction equation for the electrodes to properly describe the cooling losses from the plasma to the electrodes surface. The mathematical model was based on following assumptions.

(1) The flow was supposed to be laminar (Reynolds number $\text{Re} = \frac{DV\rho(T=10000K)}{\mu(T=10000K)} \sim 1350; D = 5 \text{mm and } V \sim 1500 \frac{m}{s}$) and weakly compressible
(2) Plasma was assumed to be in local thermodynamic equilibrium (LTE) conditions
(3) Thermodynamic and transport properties of the plasma were obtained based on LTE assumption
(4) Radiation losses were accounted using the net emission coefficient method, assuming optically thin plasma
(5) Electromagnetic phenomena were supposed to be in quasi-steady in arc plasmas
(6) Melting of electrodes was not accounted
(7) Electrode sheaths were not accounted; however, the constant electrode sheath voltage drops are considered in the calculations.

Overall, in the mathematical model, the variables of the interest were velocity ($\boldsymbol{u}$), specific enthalpy (h), electric potential (ϕ), and magnetic vector potential ($\boldsymbol{A}$). The conservation of their respective properties is expressed using below form.

$$\frac{\partial \psi}{\partial t} + \nabla \cdot (f_\psi) = S_\psi \tag{Eq 1}$$

In Eq 1, the ψ represents the volumetric conservative quantity with respect to solved variables, f_ψ indicates the flux due to advection and diffusion, and finally, the S_ψ is source/depletion term of ψ.

Table 1 shows all the governing equations expressed in their conservative form. In the table, the second row represents the conservation of mass, which includes the time (t) variation of volumetric mass (density,), , effective mass flux spatial variation, and with denoting the velocity vector of the flow field. The third row presents the

Fig. 3 (a) 3D schematic of plasma torch considered for the computation and (b) 2D schematic of 3D geometry that extended domain also included in the computation (1—rear side of the cathode, 2—inlet, 3—neutrode faces, 4—anode rear face, 5—outlet, and 6—converging nozzle faces)
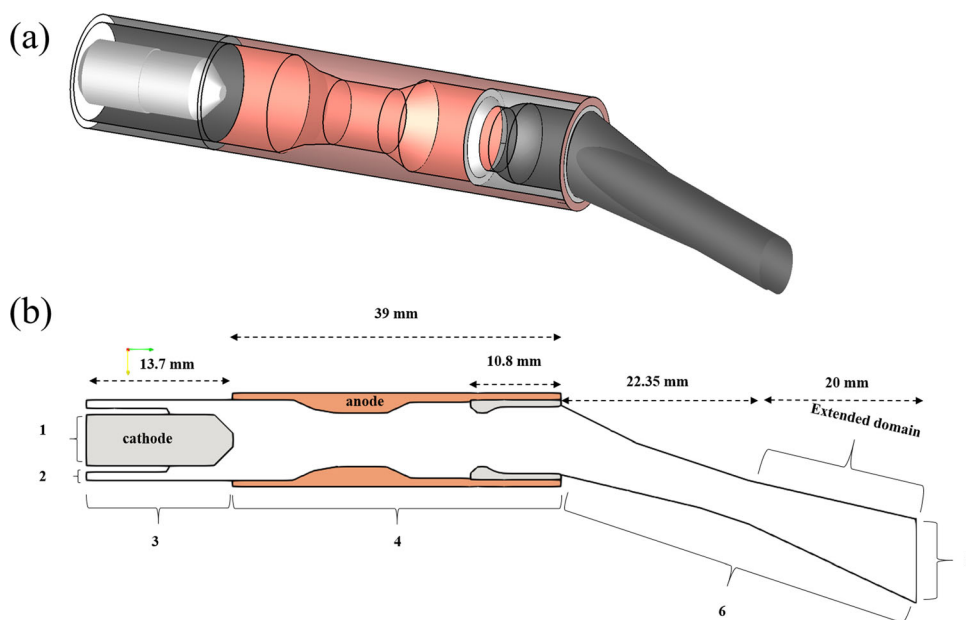
Table 1 Governing equations in the conservation form

S. No.	ψ	$\frac{\partial \psi}{\partial t}$	$\nabla \cdot \left(f_\psi \right)$	S_ψ
1	Mass, ρ	$\frac{\partial \rho}{\partial t}$	$\nabla \cdot (\rho \boldsymbol{u})$	0
2	Momentum, $\rho \boldsymbol{u}$	$\frac{\partial (\rho \boldsymbol{u})}{\partial t}$	$\nabla \cdot \left(\rho \boldsymbol{u} \otimes \boldsymbol{u} - \bar{\bar{\tau}} + p\bar{\boldsymbol{I}} \right)$	$J \times B - \Gamma_{im}\mathrm{u}$
3	Enthalpy, ρh	$\frac{\partial (\rho h)}{\partial t}$	$\nabla \cdot \left(\rho h \boldsymbol{u} - \frac{\lambda}{C_p} \right)$	$Q_J - Q_r$
4	Electric potential, $\boldsymbol{\phi}$	0	$\nabla \cdot (\sigma \nabla \phi)$	0
5	Magnetic vector potential, $\boldsymbol{A}$	0	$\nabla \cdot (\nabla \boldsymbol{A})$	$\mu_0 \boldsymbol{J}$

momentum conservation which consists of accumulation of volumetric momentum (), the momentum fluxes include the advective represents the tensor product or outer product of the vectors, diffusive (shear stress term), and the pressure contributions (—pressure and —identity tensor), and finally, the source term includes electromagnetic Lorentz force, (—electric current density and —self-induced magnetic field) and represents implicit source term dedicated to the electrode regions, which is maintained huge value, to force the null value for the velocity in the electrode regions. The next row presents the conservation of enthalpy which includes the time variation of volumetric enthalpy, (h—specific enthalpy), energy fluxes due to advection, , and diffusion, (—thermal conductivity and —specific heat) and the source terms which has contributions from the energy addition through joule heating, ( ) and energy lost through the radiation loss, (volumetric radiation loss term). Along with these three equations, to provide the description of electrical current density, magnetic field, , and electrical field, , which are required as part of the source term calculations, the model also includes appropriate Maxwell's equations in potential form. In this

list, equation 4 represents the simplified form of electric current continuity equation, , where it is expressed in the potential form by replacing with (is , —electric potential and —electrical conductivity). The transient and source terms will include the information about the charge accumulation and generation, due to the charge neutrality condition, these terms are neglected. The final equation is a potential vector description of Ampere's law that includes the , where is , and the source term informs that magnetic field generated is self-induced, as a result of electric current flow, (—magnetic permeability of free space). The shear stress () in the momentum equation is obtained through Newtonian fluid description of the plasma. Hence, the can be expressed as,

$$\bar{\bar{\tau}} = \mu \left(\nabla u + (\nabla u)^t - \frac{2}{3} (\nabla \cdot u)\bar{\bar{I}} \right) \tag{Eq 2}$$

where the μ represents laminar viscosity of the plasma.

The thermodynamic (ρ, h, C_p) and transport properties (μ, λ, and σ) were required to close the governing equations which were obtained with LTE assumption as a function of temperature. The implicit term in momentum equation allowed resolving the plasma and electrode cells

Table 2 Boundary conditions

	Velocity, u, m/s	Specific enthalpy, h, J/kg	Electric potential, ϕ, V	Magnetic vector potential, A, T-m
Cathode rear face, 1	0	27295.47 (T_{tun} = 300 K)	V_f	A using B-S Law
Inlet, 2	Q_{in}	1240 (T_{plasma} = 300 K)	$\frac{\partial(\phi)}{\partial n} = 0$	A using B-S Law
Plasma–neutrode faces, 3/converging nozzle faces, 6	0	76400 (T_{plasma} = 400 K)	$\frac{\partial(\phi)}{\partial n} = 0$	A using B-S Law
Anode rear face, 4	0	14000 ($T_{\text{anode–cop}}$ = 300 K)	0	A using B-S Law
Outlet, 5	$\frac{\partial(u)}{\partial n} = 0$	$\frac{\partial(h)}{\partial n} = 0$	$\frac{\partial(\phi)}{\partial n} = 0$	A using B-S Law

simultaneously along with the suitable interface conditions. The data of the radiation losses were taken from the literature (Ref 37).

Boundary Conditions

The boundary conditions are presented in Table 2. The null value of velocity is specified in all the electrode (1 and 4) and plasma–neutrode/converging nozzle boundaries (3 and 6), except the inlet and outlet faces. At the inlet (2), the constant value of the velocity is specified by using the gas mass flow rate Q_{in}. The normal gradient of the velocity is fixed at zero for the outlet. The specific enthalpy at the rear cathode face is 27295.47 J/kg, which corresponds to the tungsten temperature at 300 K. The gas enters through the inlet with the temperature of 300 K; hence, the specific enthalpy of plasma gas at this temperature is specified. The plasma–neutrode/converging nozzle is maintained at a specific enthalpy that corresponds to 600 K of plasma gas. The anode rear face is the side of the copper, so enthalpy of copper at 300 K. At the outlet, the null flux of the enthalpy was specified. For electric potentials, except the electrodes, all the faces were electrically neutral; hence, the null flux of electric potential was most appropriate. The cathode rear face was fixed initially at given imposed value $V_f = 300$V. The voltage imposed on the rear of the cathode was corrected at each time step with respect to the total Joule power in order to maintain the imposed electric current through the computational domain. This allowed to dynamically predict the arc voltage. The procedure for determining the electrical potential is presented in the ref (Ref 37). The anode is maintained at the ground potential; hence, the electric potential was zero. The specification of the boundary conditions of A for the magnetic vector potential equation was not easy, as the boundary values were dynamically changed during the simulation. It is worth mentioning that the magnetic vector potential is generated due to electric arc; hence, the electric arc dynamic motion will reflect in boundary values.

Hence, the boundary values were calculated using the Biot–Savart's law as it was done in Zhukovskii et al. (Ref 23, 38). The expression of boundary face value using the B-S law is shown below.

$$A_{i,\text{face}} = \frac{\mu_0}{4\pi} \sum_{j=1}^{ncells} \frac{J_j}{|r_i - r_j|} \Delta V_j \tag{Eq 3}$$

In the above equation, the $A_{i,\text{face}}$ is magnetic vector potential at ith component of A at a face of the boundaries. The summation runs for all the cells in the computational domain; j represents the index of the cell, $r_i - r_j$ is distance between the face center (i) and cell center (j), and ΔV_j is the volume of the j cell.

Thermal and Electrical Coupling Conditions Between the Regions

Along with above boundary conditions, the interface constraints for specific enthalpy and electric potential variables were crucial in ensuring the energy and electric current conservation at the region interfaces. There are mainly three types of regions in present numerical model; they are (1) cathode–plasma interface, (2) anode (A1 or A2)–plasma interface, and (3) anode (A1)–anode (A2) interface.

Cathode–plasma interface

The interface condition for the enthalpy is based on specifying constant temperature, which is calculated from the continuity of temperature (Eq. 4a) (Ref 30, 40) and conservation of conduction heat fluxes (Eq. 4b) at the interface boundary.

$$T_{i,\text{cathode}} = T_{i,\text{plasma}} \tag{Eq 4a}$$

$$\lambda_{\text{cathode}} \frac{\partial T_{i,\text{cathode}}}{\partial n} = \lambda_{\text{plasma}} \frac{\partial T_{i,\text{plasma}}}{\partial n} \tag{Eq 4b}$$

$$\lambda_{i,\text{effective}} = \frac{\lambda_{\text{cathode}}\lambda_{\text{plasma}}}{2d_{i-\text{plasma}}\lambda_{\text{cathode}} + 2d_{i-\text{cathode}}\lambda_{\text{plasma}}} \quad \text{(Eq 4c)}$$

$$Q_{i,\text{diffusion}} = -2\lambda_{i,\text{effective}}\left(T_{\text{cathode}} - T_{\text{plasma}}\right) \quad \text{(Eq 4d)}$$

In the above equations, $T_{i,\text{cathode}}$ and $T_{i,\text{plasma}}$ indicate the interface temperature of cathode and plasma regions, and λ_{cathode} and λ_{plasma} are thermal conductivity of the cathode and plasma regions, respectively. Finally, $\frac{\partial T_{i,\text{cathode}}}{\partial n}$ and $\frac{\partial T_{i,\text{plasma}}}{\partial n}$ represent the normal gradient of the temperatures from the both sides. The specification of the conduction heat flux is necessary at the boundary; hence, the effective thermal conductivity is necessary, and it is calculated using Eq 4c, which is simple harmonic mean of the neighboring cells thermal conductivities. In this equation, the $d_{i-\text{plasma}}$ and $d_{i-\text{anode}}$ are the distance between the interface to the plasma and anode neighboring cells, respectively. The resultant conduction flux at the interface can be calculated from Eq 4d, and it is specified as the heat flux boundary condition. In Eq 4d, the T_{cathode} and T_{plasma}, respectively, are the temperature of neighboring cells of cathode and plasma.

Due to the short length and time scales, the cathode sheath at the plasma boundary is not currently modeled. Zhukovskii has suggested that heat fluxes due to electric current, ion current, and surface radiation losses are associated with the 3D area near the interface, rather than being localized strictly at the interface boundary (Ref 40). To ensure appropriate heat conservation, additional heat fluxes from electron cooling, ion heating, and radiation absorption were incorporated as source terms in the energy equations for the interface cells (Ref 24, 29). To maintain dimensional consistency, these heat flux terms were multiplied by the corresponding surface area of the boundary face before being added as source terms in the energy equation. It should be noted that our numerical model takes energy sources as absolute values and automatically converts them into volumetric source terms by dividing by the respective cell volume.

The additional heat flux is given by the below expression.

$$Q_{\text{additonal}} = -J_{\text{emis}} \cdot \left(\frac{2k_b}{e}T_{\text{cathode}} + \frac{\Phi_W}{e}\right) + J_{\text{ions}}$$
$$\cdot \left(\frac{5k_b}{2e}T_{\text{plasma}} + \frac{\Phi_i}{e} + U_C\right) + Q_{\text{rad}-\text{cathode}}$$
$$\text{(Eq 5)}$$

In Eq 5, the first term on the right-hand side represents the electron cooling and the other one indicates the heating due to thermionic heating. The J_{emis} represents the thermionic emission of electron flux, which is obtained from the Richard–Dushman law supplemented with Schottky correction.

$$J_{\text{emis}} = A_G T_{\text{cathode}}^2 \exp\left(-\frac{\Phi_W - \Delta W}{kT_{\text{cathode}}}\right) \quad \text{(Eq 6)}$$

where $A_G = 6 \times 10^5 Am^{-2}s^{-2}$, $\Phi_W = 2.5\text{eV}$ is cathode material work function corresponds to the tungsten with lanthanum oxide dopant and ΔW is reduction in the work function given by Schottky correction and the value used here was 0.05 eV.

The second term in Eq 5 indicates the heat flux due to the thermionic heating of the ions. The ion current density J_{ions} is given by subtracting the thermionic flux of electron density from the calculated interface electrical current density. The $\Phi_i = 13.6eV$ is ionization potential of the hydrogen (smallest of the species present) and $U_C = 10$ V is cathode fall voltage. The $Q_{\text{rad}-\text{cathode}}$ represents the radiation absorbed at the cathode surface through the plasma emission. The calculation of $Q_{\text{rad}-\text{cathode}}$ is given in the ref (Ref 40).

Similar to the thermal coupling, the electrical coupling is also applied; hence, the interface constant electric potential was obtained from ensuring the continuity of the electric potential as well as conserving the electric current.

$$\phi_{i,\text{cathode}} = \phi_{i,\text{plasma}} \quad \text{(Eq 7a)}$$

$$\sigma_{\text{cathode}} \frac{\partial \phi_{i,\text{cathode}}}{\partial n} = \sigma_{\text{plasma}} \frac{\partial \phi_{i,\text{plasma}}}{\partial n} \quad \text{(Eq 7b)}$$

In the above equations, ϕ_{cathode} and ϕ_{plasma} indicate the interface electric potential of cathode and plasma regions, and σ_{cathode} and σ_{plasma} are electrical conductivity of the cathode and plasma regions, respectively. Finally, the $\frac{\partial \phi_{\text{cathode}}}{\partial n}$ and $\frac{\partial \phi_{\text{plasma}}}{\partial n}$ represent the normal gradient of the electric potentials from the both sides.

Anode–plasma interface

The thermal and electric coupling between the anode–plasma interface was similar to that of cathode-plasma interface, except the cathode properties were replaced by the anode properties in Eq 4a, 4b,4c, 4d, 7a and 7b. Especially, the main difference comes in specifying the additional heal flux which was mainly due to the electron condensation and radiation absorption from plasma column. The heat flux due to electron condensation is given by Eq 8.

$$Q_{\text{anode}} = J_{\text{elec}} \cdot \left(\frac{5k_b}{2e}T_{\text{elec}} + \frac{\Phi_A}{e} + U_a\right) \quad \text{(Eq 8)}$$

where J_{elec} is calculated electrical current density at the plasma–anode interface, Φ_A represents the anode material work function and U_a is anode fall voltage. The value of

Φ_A is 2.5 eV (tungsten with lanthanum oxide dopant), and the value of U_a is 3 V. The J_{elec} is obtained from the below expression:

$$J_{elec} = -\frac{\sigma_{anode}\sigma_{plasma}}{2d_{i-plasma}\sigma_{anode} + 2d_{i-anode}\sigma_{plasma}}(\phi_{anode,c} - \phi_{plasma,c})$$

(Eq 9)

In the above equation, the σ_{anode} and σ_{plasma} represent the electrical conductivities of anode and plasma cells next to their interface, $d_{i-plasma}$ and $d_{i-anode}$ indicate the respective distance between interface and plasma/anode cell centers, and finally, $\phi_{anode,c}$ and $\phi_{plasma,c}$ are the electric potentials interface cells (anode/plasma). In addition to the anode condensation heat flux, the radiation from the plasma $Qrad-anode$ is also added as additional flux. The procedure for calculation of the radiation flux is provided in the ref (Ref 40).

Anode-T–Anode-C interface

The thermal and electrical coupling of the interface between the anode-T and anode-C is similar to that of above two cases.

Arc Breakdown and Restriking

As discussed in the introduction section, each plasma torch of the Axial III Plus device operates with a high gas flow rate, using an argon–hydrogen gas mixture and low arc current intensity (Ref 5). Under these operating conditions, the electric arc inside the torch operates in the so-called restrike mode (Ref 30-32, 40), characterized by rather large arc voltage fluctuations (Ref 12). These fluctuations are caused by the movement of the anode arc attachment in the downstream direction, primarily associated with an imbalance between fluid dynamic drag and electromagnetic forces at the anode attachment location. As a result, it gradually stretches the arc column length and increases the torch voltage (Ref 40). Subsequently, due to arc breakdown in the upstream direction, a new anode attachment forms, rapidly reducing the arc column length and causing a rapid drop in arc voltage δ_v (Ref 35, 41). The time-dependent evolution of the arc voltage is characterized by a sawtooth-shaped voltage pattern, showing linear increasing ramps followed by sudden negative jumps δ_v. This pattern repeats in a few to tens of kilohertz range.

The mathematical model used in this work was not enough accurate to predict the restrike mode of the electric arc inside the plasma torch. For example, without the restrike model, the solution of the basic numerical model can only describe the electric arc movement without any electric arc column breakdown; consequently, the anode arc attachment moved continuously to the downstream direction and stayed at the end of the anode nozzle; hence, the temperature and velocity profiles predicted were not quite real and correct. The present restrike model was based on the predicted average radial electric field at the electric column edges or cold boundary layer. For numerical purpose, the electric arc fringes can be described by the group of cells whose temperatures were around 7000 K which has a sufficient electric conductivity for electric current penetration, together with highest electric conductivity variation with temperature for ensuring end of the arc column. Rat and Coudert have proposed the critical temperature of the cold boundary layer based on the thermodynamic and transport properties of different gases, which is between 6000 and 7000 K and corresponds to an electrical conduction threshold (Ref 42).

The basic principle of this model was that, at every time step, the mean radial electric field (Eq 10) was monitored and checked whether it goes beyond the certain threshold field, E_b. For instance, if it is that case, at the location of cell, where this condition is satisfied, a high artificial electric conductivity column is applied to mimic the arc column breakdown in the upstream direction. In this model, the mean electric field $E_{r,mean}$ was calculated using the following formula.

$$E_{r,mean} = \frac{\phi_{7000K} - \phi_{anode}}{\Delta r}$$

(Eq 10)

where in the above equation, the ϕ_{7000K} is electric potential of the cell with 7000 K temperature, ϕ_{anode} is the anode electric potential fixed at 0 in the present simulations. Finally, the Δr represents the radial distance between the cell and the closest inner surface of the anode, i.e., the cold boundary layer thickness. The electric conductivity of arc column is 159 S/m corresponding to the temperature of 7000 K for argon and hydrogen mixture used in the present study. The angular and axial thicknesses of the column were 20° and 0.8 mm, respectively. The threshold field, E_b, is a crucial parameter that can be varied to find the optimized value in fitting the experimental measurements, such as the fluctuations of the electric arc voltages, average electric power dissipated and thermal efficiency. For the better understanding of this model, the working schematic of the breakdown model is presented in Fig. 4. The first sub-Fig. 4(a) displays a typical electric arc configuration before the initiating the arc column. In this figure, we can observe the stationary and steady cathode attachment and unsteady anode arc attachment, which is almost reached close to the end of the anode nozzle. In the absence of the restrike model, the anode arc attachment reaches the end of the nozzle and stays there, which is not practically observed.

However, if the restrike model is present, which is active at all the time steps; particularly, at this instance, the algorithm will check the plasma cells with the temperature

Fig. 4 Schematic of the restrike process using the restrike model; (a) the fully developed arc just before restrike, (b) the fully developed arc with new artificial column (red colored column) in the upstream direction and the isotherms of the 7000 K; and (c) new arc configuration after just restrike has passed
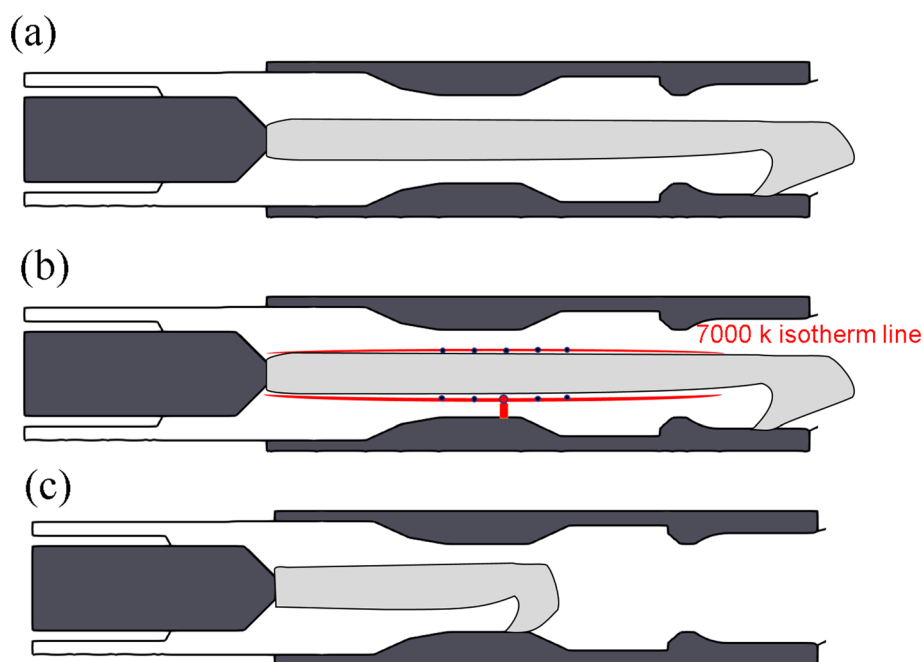
between 6950 and 7050 K (check the red color isotherm in Fig. 4(b), for their local electric potential and calculates the mean radial electric field using Eq. 8. Subsequently, the mean radial electric field is compared with given E_b; if it goes beyond this value, the algorithm will be ready to initiate the artificial electric conductivity column. In most cases, there are multiple cells satisfying this condition (similar to the blue circled points of Fig. 4b); hence, the cell location with the maximum radial electric field (red circled over the blue ones in Fig. 4b) was chosen. At this location, the artificial conductivity column was imposed, similar to the red colored column shown in Fig. 4(b). Figure 4(c) shows the configuration of developed electric arc after the establishing the new arc attachment due to restrike model.

The value of 7000 K has been selected based on previous work by Moreau et al. (Ref 18), where it was identified as a critical temperature at which the electrical conductivity of the arc column approaches zero for various gases, including argon, hydrogen, and their mixtures. This is illustrated in Fig. S1, which shows radial profiles of axial current density and temperature at the lower diameter section of the anode at $z = 25$ mm. These profiles typically exhibit asymmetry in the radial direction, with the current density approaching zero at different radii—specifically, at $r = -1.95$ mm and $r = 1.48$ mm. Importantly, both of these points correspond precisely to the 7000 K isotherm, underscoring its significance in describing the cold boundary layer of the plasma.

We further examined the results using two other isotherms: 8000 K and 5000 K. For the 8000 K isotherm, our

numerical model encountered divergence issues, likely due to the sensitivity of the electric potential solver to the artificial conductivity imposed along the electric current path. In contrast, selecting the 5000 K isotherm yielded more stable results without numerical issues. However, the starting radial point of the artificial column was significantly distant from the arc column, preventing a connection and resulting in downstream dragging of the electric arc attachment without any restrike. These findings indicate that the 7000 K isotherm is the most appropriate choice for describing the cold boundary layer compared to the other temperatures.

The choice of E_b is based on the critical electric field that must be exceeded to disrupt the cold boundary layer. Coudert et al. (Ref 43) demonstrated that the jump amplitude (δ_v) is proportional to the thickness of the cold boundary layer ($\Delta R = R - r_e$, where R represents the nozzle radius and r_e denotes the arc column radius). This finding underscores the presence of a constant "critical" field of approximately 20 kV/m, beyond which the cold boundary layer experiences electrical breakdown. This critical field value is one or two orders of magnitude lower than what is typically observed for electrical disruption in a cold gas.

More recently, a thermal instability was put forward as possible mechanism. Experimental observations (Ref 33) have indeed shown that a relatively small fraction of the main arc current (i.e., a residue or leakage current) flows upstream of the main arc attachment through the cold boundary layer, indicating the existence of a non-thermal diffuse glow discharge. Nemchinsky (Ref 35) proposed a simplified thermodynamic non-equilibrium [i.e., non-local

thermodynamic equilibrium (NLTE)] model considering the unbalance between ionization and recombination process in the cold boundary layer. Using this model, he showed that the leakage radial current is determined by a very low electrical conductivity of the cold anode layer. When the main arc attachment moves downstream, the voltage across the anode boundary layer increases. Therefore, the upstream leakage current increases and warms up the anode layer; its electrical conductivity rises and thus allows an increasing fraction of the total current to redistribute upstream until a new anode spot develops. This overheating instability was found for critical electric field around 10-50 kV/m.

Finally, in the present study related to axial 3 + plasma torch, the disruptive voltage needed to break the cold boundary layer should be higher than that encountered in other old legacy APS plasma torches, due to the anode geometry and the operating parameters used (high gas flow rate and low arc current intensity) leading to thicker cold boundary layer. As a consequence, the averaged value of the critical electric field was set around 10^5 V/m in the current work.

Computational Approach

The final numerical model, which combines the governing equations shown in Table 1, boundary conditions shown in Table 2 and interface conditions presented in Section 2.4, is solved using the open-source CFD code code_saturne which is developed by Electricité de France (EDF). Even if practical experience suggests that the Axial III is almost never operated without nitrogen for the production of coatings, especially in suspension plasma spray, it has to be noted that thermodynamic and transport properties are a prerequisite to any plasma torch numerical simulation. LTE gas properties are widely available for practically all gases used in plasma spraying (Ar, H_2, N_2, H_2O, He, CH_4) and their binary and ternary mixtures (Ar-H_2, Ar-He, Ar-O_2, Ar-N_2, air-N_2, air-Ar, air-O_2, air-CH_4, Ar-H_2-He, Ar-H_2-Cu) (Ref 37, 44-47). However, to the best knowledge of the authors, data related to ternary mixtures with Ar-N_2-H_2 various composition and temperatures up to 30.000 K are still missing.

The operating conditions consist in an arc current intensity of 200 A, a plasma forming gas mixture of argon and hydrogen (75%-25% vol) and a mass flow rate of 100 Nl/min (0.0023 kg/s).

The meshing of the computational domain is carried out using the ICEM CFD software. The total number of cells in each region is: (1) cathode—250 k; (2) plasma—1500 k; (3) anode-T—48.6 k and (4) anode-C—145 k. The cell numbers are optimized to provide best compromise between the convergence, solution accuracy, and CPU

runtime. The cells are hexahedral, and the largest cell size in the whole mesh is 500 mµ. The sizes of the plasma cells, neighbor to the cathode and anode regions interface, are maintained at 50 µm and 25 µm, respectively. These cells and their thickness are important in providing the artificial higher electric conductivity to allow the flow of electric current.

The simulation was performed using 28 core Intel Xeon Gold 6258 R CPU @ 2.75 GHz and uses the 24 GB RAM. The numerical simulations were carried out with time step of 0.08 sµ.

Results and Discussion

Initially, at $t = 0$, to replicate the arc initiation, an artificial '¬'-shaped temperature column (7000 K) was established between the cathode tip and a specific location on the internal surface of the anode nozzle. Similar methods have been utilized in numerous previous simulations (Ref 21, 24, 40), and detailed information on the present method can be found in Zhukovskii et al. (Ref 40). The simulations were conducted for a minimum duration of 5000 time steps to mitigate initial and boundary effects on the simulation results and ensure that several plasma jet flows had exited the domain.

Prediction of Magnetic Field inside the Plasma Torch

In plasma torch modeling, accurately predicting the magnetic field is crucial (Ref 39). It enables a precise description of the Lorentz force and the self-constriction of the arc plasma, known as the pinch effect. For example, overpredicting the arc constriction leads to increased joule heat dissipation (i.e., power), resulting in differing spatially temperature and velocity profiles. Consequently, larger gradients in temperature and velocity can alter the electric field calculated at the electric arc fringes, a crucial parameter in the restrike model used to replicate electric arc breakdown during the restrike mode. Consequently, the restrike frequency and the average power of the torch are influenced.

The present model employs Ampere's law in potential vector formulation (see Table 1), along with the boundary conditions shown in Eq. 3, to obtain the spatial distribution of the magnetic vector potential necessary for magnetic field calculation. Previous studies (Ref 21, 48, 49) have commonly utilized the null flux condition for the magnetic vector potential at boundaries, a method that is straightforward to implement. However, Zhukovskii et al. (Ref 39) demonstrated that this technique leads to incorrect predictions of the magnetic field for a SinplexPro plasma

torch. They proposed using the Biot–Savart law to calculate the magnetic vector potential at boundaries. The same approach has been adopted for the present work with the Axial III Plus geometry.

In this technique, the challenging step involved obtaining the boundary value using Eq. 3, which necessitated the volume integration of the electric current density at every time step, crucial for unsteady arcs (i.e., the electric current distribution over time), particularly for APS torches (F4, 3 MB, 9 MB). This resulted in significantly higher computational time and was practically unfeasible for the plasma torch of the Axial III Plus computational domain, which required a large number of cells. Therefore, in the present simulations, the boundary value was calculated every 100 time steps, under the assumption that the effect of spatial variation of electric current density on the boundary value during this time span was negligible.

Figure 5 presents the typical predicted instantaneous azimuthal magnetic field inside the plasma torch, along with the electrical current density profile over the cathode surface (on the right-hand side of the figure). It is noted that for the longitudinal electric current lines, particularly occurring in this case with straight gas flows, the generated self-magnetic field exhibits rotational behavior along the lines, hence the azimuthal component is dominant. Overall, at the center of the arc column ($r = 0$) at any axial location, as displayed along the central axis, the magnetic field is zero. However, it was observed to rise radially until a specific radial location, R, corresponding to the arc column radius r_e; from there, the magnetic field decreases rapidly. This is a common profile of self-created magnetic fields, which can also be observed and reproduced in a simple case with an active electrically conductive wire placed in open air.

Two prominent characteristics of the magnetic field in arc plasma torches are observed at the cathode and anode attachment locations. Firstly, at the cathode tip, the magnetic field value increases radially from 0 to 0.0358 T, which is higher compared to other axial locations due to higher electric current densities at the cathode tip. The figure on the right-hand side of Fig. 5 illustrates a nearly flat profile of the electrical current density, reaching approximately $7 \times 10^7 \text{A/m}^2$, with the electrical current density increasing to $1.3 \times 10^8 \text{A/m}^2$ at the edges of the cathode tip. Secondly, there is an increase in the local magnetic field at the inner curvature of the arc current path as it bends from the longitudinal direction and passes through the anode nozzle.

In addition to these characteristics, another important feature specific to the Axial III Plus geometry is the radial maxima of the magnetic field along the longitudinal direction, inversely proportional to the internal diameter of the anode nozzle. This can be attributed to the constriction/expansion of the electric arc as it passes through the lower/higher diameter of the anode nozzle, reflecting in the radial profiles of the azimuthal magnetic field. It is noteworthy that the maximum values of the magnetic field at the cathode tip for the Axial III Plus torch (0.0358 T) are lower than those obtained for the Simplex Pro and F4 plasma torches: 0.05 T (for an arc current intensity of 500 A, 60 slpm Ar, 9 mm nozzle diameter) (Ref 29) and 0.09 T (for a current intensity of 600 A, 45/15 Ar-H$_2$, 6 mm nozzle diameter), respectively (Ref 23). This illustrates the model's consistent prediction of the influence of operating parameters, particularly arc current intensity and plasma torch geometry, on the evolution of the magnetic field inside the nozzle of a plasma torch.

Prediction of Electrode Temperatures

Alongside predicting the magnetic field, solving for electrode temperatures is crucial for estimating the accurate heat losses to the electrodes, thereby influencing the dynamics of the arc under restrike mode. In cases where there is an overprediction of heat losses to the anode, it may increase the cold boundary layer thickness between the arc column and the anode inner surface. Consequently,

Fig. 5 The azimuthal magnetic field predicted inside the torch using the approach of B-S law.

$J(A/m^2)$

$B_\theta (T)$

0.0000 0.005 0.01 0.015 0.02 0.025 0.03 0.035 0.0417
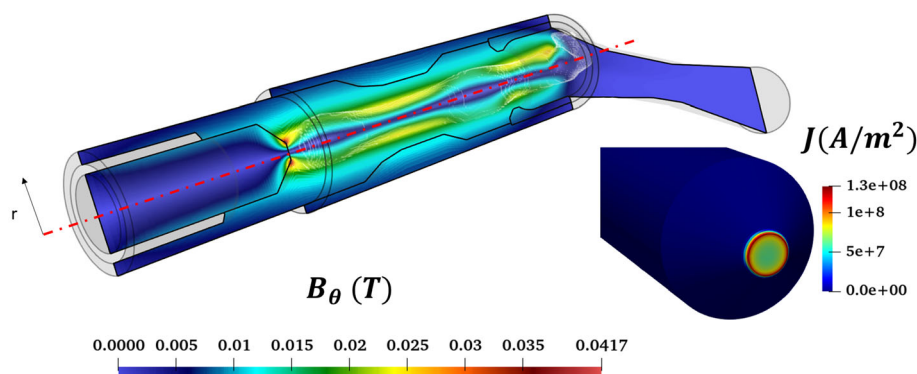
this can lead to the overprediction of the radial electric field at the arc fringes.

Figure 6 illustrates the instantaneous temperatures of the cathode and anode alongside the electric arc. The electric arc shown in this figure was generated by grouping all plasma cells containing electric current density values between $2 \times 10^6 A/m^2$ and $4 \times 10^8 A/m^2$. These current density values were selected arbitrarily to cover the maximum current density around the cathode tip, estimated at approximately $1.2 \times 10^8 A/m^2$, with the minimum value chosen to be less than 2% of the maximum value, at $2 \times 10^6 A/m^2$.

The rear end of the cathode was set at 300 K as a boundary condition, and the temperature was observed to increase continuously along the cathode length until it reached the cathode tip, where the temperature was nearly 3400 K. Similar temperatures around 3400 K are expected with tungsten cathodes doped with lanthanum oxide. Regarding the anode, temperatures ranged between 300 K (outer surface) and 600 K (inner surface), except near the anode arc attachment. The temperature of the anode inner surface was inversely proportional to the internal diameter of the anode nozzle, varying from 300 to 420 K as the diameter changed from 9.5 to 5.8 mm. However, at the anode arc attachment, the temperature was relatively higher, reaching approximately 600 K.

It is understood that the higher temperature at the anode surface is a result of localized current density heating, which is transported to the anode surface through various means, including thermal diffusion at the plasma–anode interface and absorption of radiation from the plasma. Additionally, heat is generated from electron condensation at the anode surface. However, the temperature at the anode arc attachment is lower than the cathode tip temperature, primarily due to the short residence time of the arc attachment at that particular location on the anode surface. This short residence time is mainly a result of the

continuous downstream dragging of the arc attachment. For clarity, the temperature traces for the previous anode attachment can be observed just before the present attachment in Fig. 6.

Experimental measurements of anode surface temperatures pose challenges, particularly for anode nozzles of this nature. However, employing a non-equilibrium model, Liang and Groll (Ref 30) demonstrated that, in a similar plasma torch scenario (Praxair SG-100 plasma spray) using pure argon, maximum anode surface temperatures of around 1000 K were observed with an arc current of 700A. This represented an increase of approximately 500 K from the imposed cooling temperature of 500 K. It is anticipated that for lower arc currents (approximately 200 A), the temperature rise would be less than 500 K. Similarly, in the present case, a temperature rise of 300 K is observed. Although this value appears consistent, it may be underpredicted compared to the pure argon case, which produces a diffused arc attachment. Consequently, the maximum anode temperatures in the present case are relatively higher.

Figure 7 provides a detailed examination of the density and temperature distribution within the two layers of tungsten and copper at the anode. The density of the tungsten layer is 19200 kg/m^3, while that of copper is approximately half at 8940 kg/m^3. Therefore, ensuring proper thermal coupling at the interface is essential to maintain energy flow between the layers. In Fig. 7(b), the temperature variation within the two layers is depicted. It is observed that the temperature change is continuous. Along sectional line A, for instance, the temperature of the tungsten region adjacent to the plasma side is 418 K. This temperature gradually decreases and reaches approximately 355 K at the interface layer. From there, the temperature decreases further within the copper region until it reaches the opposite end, where a constant temperature of 300 K is maintained as a boundary condition.

Fig. 6 Sectional view of the anode and cathode temperature distribution along with the electric arc ($J = 2 \times 10^6 A/m^2$–$4 \times 10^8 A/m^2$)
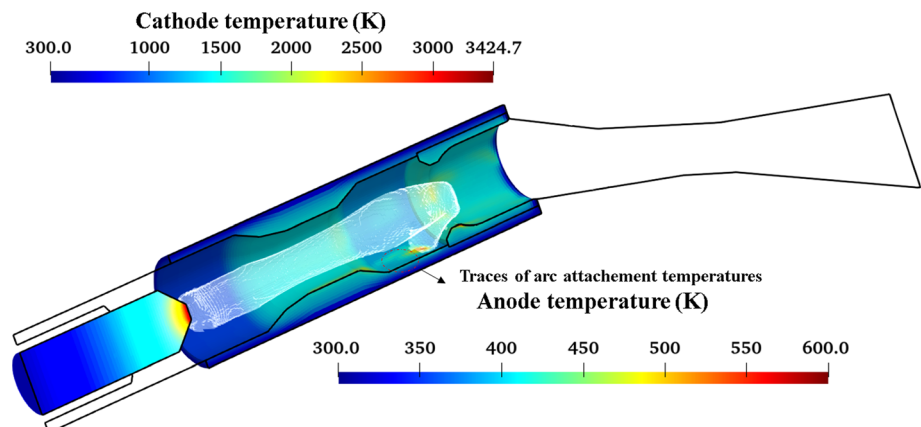
Fig. 7 Sectional view of the anode layer (a) density and (b) temperature
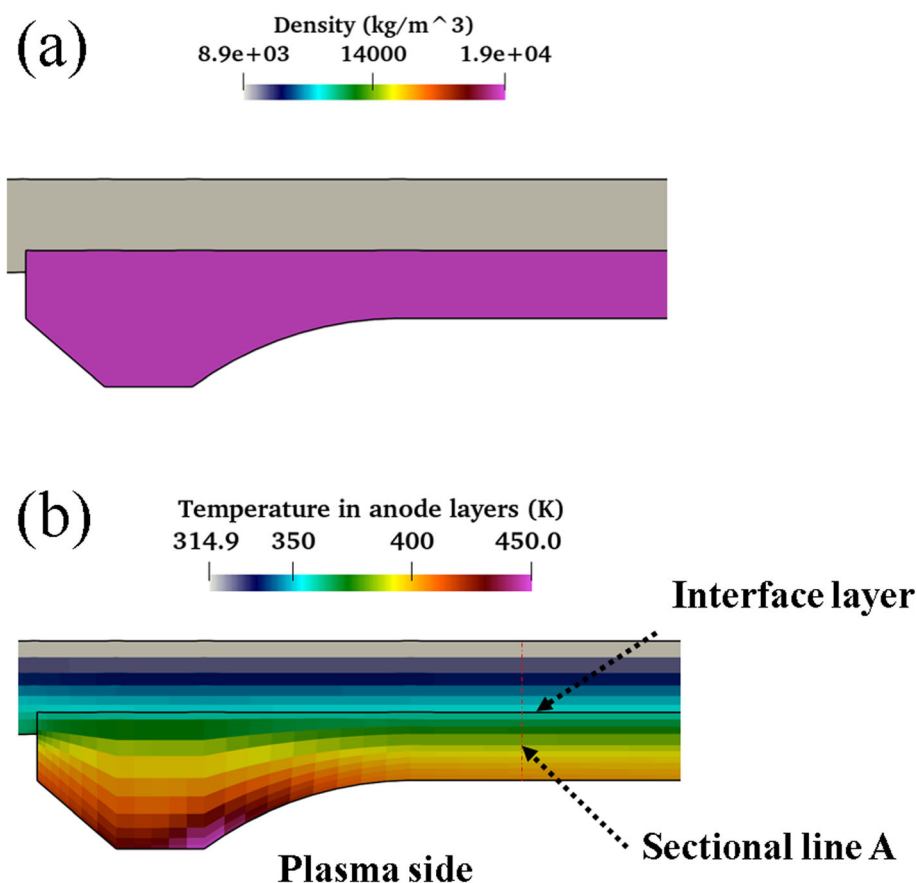
Time Evolution of Arc Voltage and Gas Characteristics at Torch Exit

Figure 8 illustrates the results of the restrike model, showcasing the electric arc along with temperature distributions across the cathode and anode regions, similar to Fig. 4. Additionally, the corresponding variation of arc voltage with time is depicted at the bottom. The arc voltage, defined as the difference between the anode and cathode electric potentials, is a crucial parameter. It is directly proportional to the arc length, aiding in validation against experimental measurements.

For clarity, only the temperature distributions over one half of the geometry are displayed. All simulations, including the case depicted in Fig. 8, were conducted over a minimum of 5000 time steps to account for dissipation effects associated with initial and boundary conditions. In this particular case, the threshold field value (E_b) for the restrike model was set to 1×10^5 V/m, nearly two times higher than the value used in the Moreau et al. (Ref 18). This adjustment was made considering the operating parameters of the Axial III Plus torch: a higher gas flow rate of 100 slpm, a 75-25% Ar-H$_2$ gas mixture (molecular gas mixture), and a lower arc current intensity of 200 A. These parameters are expected to result in a relatively thick cold boundary layer, thus necessitating a stronger disruptive arc voltage (average electric field) to electrically break it (Ref 43).

In Fig. 8(a) (at time step − 13150), the arc attachment on the anode is observed at $z = 20.8$ mm (as indicated by the black arrow). This position corresponds to the end of the converging part of the copper anode nozzle inner surface, which maintains a constant inner diameter of around 5.9 mm from this point onwards, extending till $z = 25.8$ mm (as indicated by the red arrow). At this time step, the arc voltage reaches its lowest value of 72.5 V (marked as point 'a' in the Voltage vs time plot). As time progresses, the anode attachment moves downstream due to a combination of incoming fluid drag and asymmetric electromagnetic force resulting from the curvature of the arc at the anode attachment point.

Figure 8(b) illustrates the downstream movement of the arc attachment, reaching $z = 25.8$ mm (as indicated by the black arrow), where the ramping up of the anode inner diameter commences. Subsequently, Fig. 8(c) displays the arc configuration at the conclusion of the ramp of the anode inner surface, with the attachment at $z = 29.2$ mm and the corresponding voltage increasing from 96.5 V (point 'b') to 109.5 V (point 'c'). The differing slopes of lines 'ab' and 'bc' reflect variations in the anode inner diameter

Fig. 8 Snapshots of the electric arc during a restrike period together with the electrode temperatures; the bottom figure represents the arc voltage variation during the restrike period
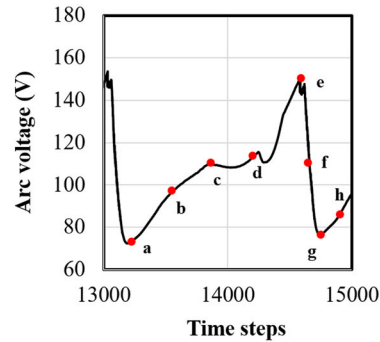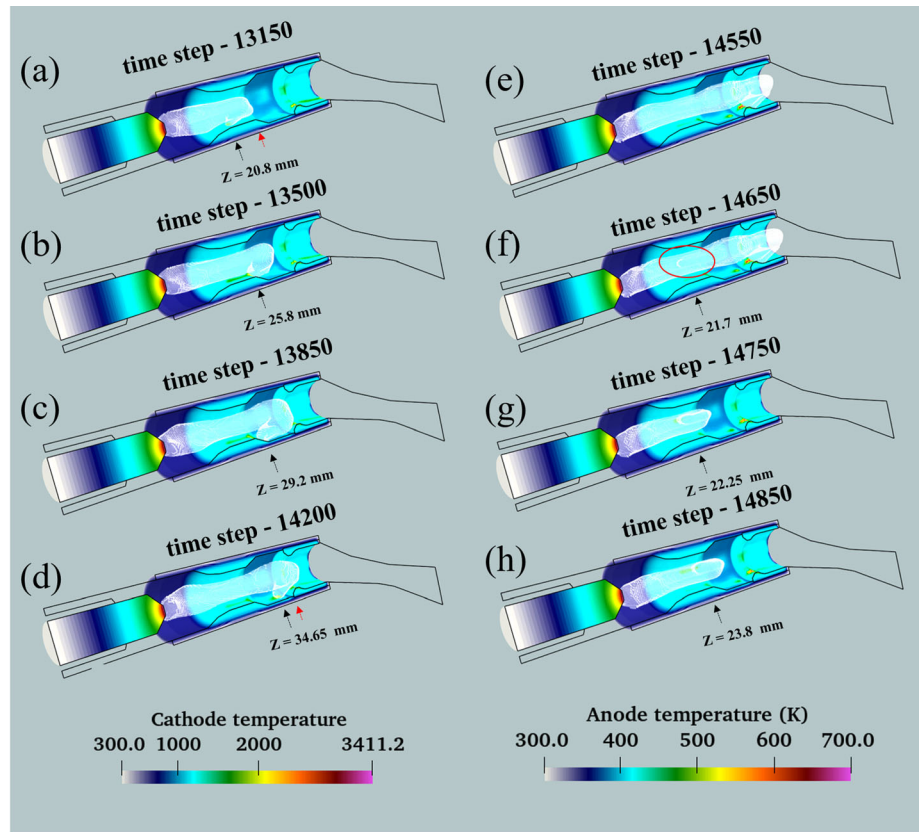
during these phases. It is noteworthy that, in the case of torches with a constant diameter, such as the F4, the slopes of lines 'ab' and 'bc' are typically identical, resulting in a purely linear relationship.

Further downstream movement of the anode attachment is observed until it reaches ($z = 34.65$ mm). The voltage corresponding to this point is 114.7 V (point 'd'). The voltage variation between points 'c' and 'd' appears unusual, exhibiting a nonlinear trend despite the constant diameter in this region. Additionally, the voltage increases from point 'c' to point 'd' is unusually lower compared to the previous phases (a to b and b to c). This peculiar variation may be attributed to non-linear variations in fluid drag associated with velocity streamlines bounded by lower anode diameter sections from either side (See two

red color arrows: one in 'a' and other in 'd'). Specifically, as the anode attachment progresses downstream, the interaction between the electric arc and the fluid flow can lead to complex behaviors in the plasma dynamics, affecting the voltage characteristics. The constant diameter might contribute to stabilizing effects or variations in local plasma properties, such as temperature and density gradients, influencing the overall voltage response.

Following this, as the anode attachment climbs up the step associated with the tungsten block mounted on the copper block, there is a small dip in the voltage vs time profile, indicating a slight reduction in arc length due to the jump of the arc attachment onto the tungsten. Once the climbing is complete, the arc attachment is intensely pushed downstream due to fluid drag, resulting in a steep

variation in voltage between points 'd' and 'e', reaching a peak value of nearly 148 V at time step 14550.

As time progresses, a new attachment location is determined by the restrike model algorithm, satisfying the criterion $E_{r,meanb} > E_b$. This new attachment, highlighted with a red circle in Fig. 8(f), is imposed at $z = 21.7$ mm, causing a rapid drop in voltage from point 'e' to point 'f', reaching approximately 108 V. The electric arc establishes its new configuration, with the old attachment automatically disappearing. Figure 8(g) displays the completely developed new arc configuration, the corresponding voltage reached to lowest value (73.6 V) during this restrike cycle.

This behavior continues over time, with the arc attachment moving downstream and arc breakdown occurring due to the restrike model. Figure 8(h) illustrates the downstream movement of the anode attachment after establishing its new configuration, with a corresponding voltage of 87 V and arc attachment location at $z = 23.8$ mm.

Figure 9 illustrates the instantaneous temperature (a, b) and velocity (a', b') profiles of the plasma and the electrode sections during the restrike period discussed in Fig. 8. It demonstrates that the temperature fields inside the torch exhibit significant three-dimensional features, and due to the natural fluctuations of the arc root attachment at the anode surface, the resulting plasma jets consist of successive "puffs". For clarity, only two-time steps (13500 and 14550) are displayed here: the first (13500) corresponds to a fully developed arc configuration after the formation of a new anode arc attachment, corresponding to point 'b' in the voltage vs time profile, while the last (14550) represents the arc configuration just before arc breakdown, corresponding to point 'e' in the voltage vs time profile.

At both time steps, the maximum temperature is nearly 21 400 K near the cathode tip. In both profiles, the high-temperature plasma jet, generated by the joule heating of the plasma gas by the electric arc, is evident, surrounded by a cold boundary layer near the anode surface. The influence of the anode arc column at the anode attachment can also be observed in both temperature profiles.

It is evident that there is a variation in the lengths of the high-temperature plasma jets between the two-time steps due to the variation in the length of the electric arc; thus, case 'b' is associated with a lengthier high-temperature jet, and higher exit temperatures are expected accordingly. Similarly, the velocity profiles exhibit similar behavior, indicating that case 'b' has the lengthier jet. Although the maximal temperatures for the shown time steps are nearly the same, this consistency is not reflected in the magnitudes of maximal velocities. The maximal velocities are 1920 m/s and 2420 m/s for time steps 13500 (case 'a') and 14550 (case 'b'), respectively. In both cases, the velocity magnitude continues to increase along the arc column length. This behavior can be understood by observing the self-constriction of the electric arc due to the magnetic field, which compresses the arc column along its length, resulting in the continued rise in velocity magnitude until the end of the electric arc. Since case 'b' has a longer electric arc length, it exhibits a maximal velocity.

So far, we have examined the results of electric arc behavior under the restrike model and the corresponding time-dependent voltage profile, temperature, and velocity profiles of the plasma torch for a case with a single E_b. Hence, it was reasonable to examine the restrike nature of the electric arc for different E_b values to understand their impact on the important operational parameters of the plasma torch, particularly the mean arc voltages, voltage jump amplitudes, and the mean lifetimes of the arc spot.

Fig. 9 Sectional view of temperature (a, b) and velocities (a', b') along the computational domain length for different time step; (a, a') time step—13500 and (b, b') time step—14550

Temperature (K)
300.0 5000 10000 15000 21000.0

Velocity Magnitude (m/s)
0.0 500 1000 1500 2400.0
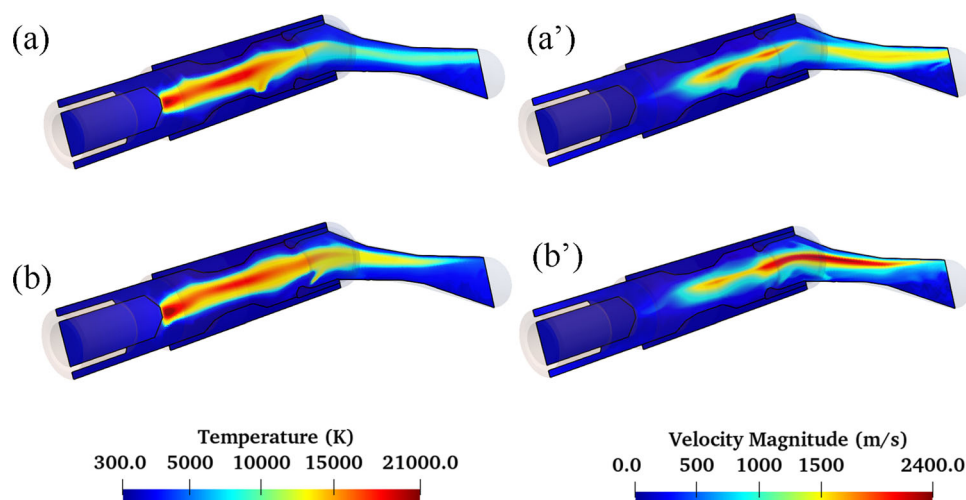
These values could be measured experimentally and compared with those estimated by numerical simulation to validate the model.

The simulations have been carried out with two different E_b values to analyze their influence on the frequency of the restrike as well as the time-averaged voltage of the electric arc. The mean lifetime of the arc spot can be obtained by averaging the time span between two minima of the arc voltage versus time curve for the last 10 periods, and it can be used to calculate the mean frequency of the restrike process or voltage curve by taking the inverse.
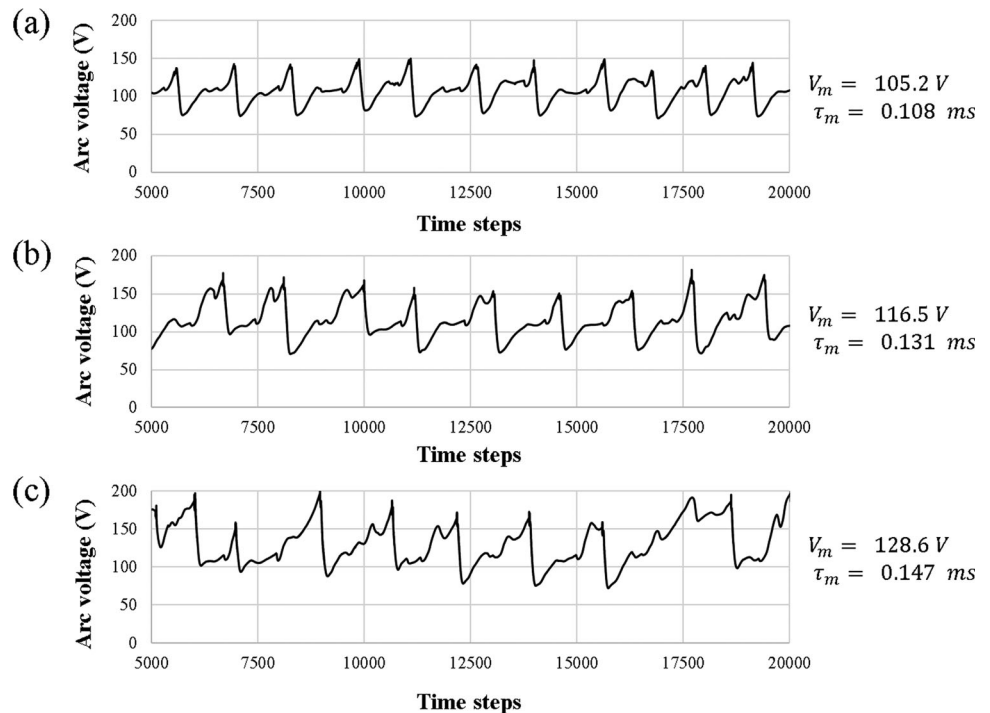
Figure 10(a), (b) and (c) presents the time-dependent arc voltage profiles for three values of E_b: 0.8×10^5 V/m, 1×10^5 V/m and 1.2×10^5 V/m, respectively. At the lower value of 0.8×10^5 V/m, the typical voltage profile shape for the single period discussed in Fig. 8 (for a longer duration shown in Fig. 10b) is also reflected here as well. The difference can be seen only in the reduction of mean arc voltage and the mean arc spot lifetimes, which are, respectively, 105.2 V and 0.108 ms. For the case of 1×10^5 V/m shown in Fig. 10(b), the mean values were, respectively, 116.5 V and 0.131 ms. This trend can be understood from the threshold value of field E_b that acts as a cutoff for the mean arc length (proportional to mean voltage and mean arc spot time) because the radial electric field generated at the arc fringes is directly proportional to the arc length.

Similar characteristics apply to the result shown in Fig. 10(c) for the higher value of E_b. The respective mean arc voltage and arc spot times increased to 128.6 V and 0.147 ms, respectively. The mean jump amplitudes of the three E_b values are nearly 64 V, 87 V, and 105 V, respectively. An important observation is that as the E_b value increases, the single period voltage profile cannot be exactly reproduced for all the periods. This discrepancy can be clearly observed in the voltage curve shown for Fig. 10(c). It may be associated with many complex factors, such as electric arc and plasma fluctuations, and the curvature of the electric arc itself. In addition to these factors, in the present case with the Axial III plus geometry, it may also arise from the variation of the internal diameter of the anode, which varies significantly along the torch length, thereby modifying the cold boundary layer thickness and the locations of the radial electric field detected at the arc fringes. The mean voltage values are helpful in estimating the power dissipated in the plasma torch, by multiplying it with the operating arc current imposed.

The energy balance of the torch for three different E_b values is presented in Table 3. The only source of energy is the joule heating from the electric arc which was calculated by integrating the volumetric joule heating source term across all plasma cells (up to the exit at $z = 0.069$ mm). Then the resultant value was time-averaged over a minimum of ten complete restrike periods. Regarding energy losses, the primary source is radiation emitted by the plasma to its surroundings. This radiation loss is determined by integrating volumetric radiation losses across all plasma volume cells up to the actual exit point of the torch

Fig. 10 Time-dependent voltage variation during the restrike process for three different Eb's; (a) 0.8×10^5 V/m, (b) 1×10^5 V/m and (c) 1.2×10^5 V/m

(a) $V_m = 105.2\ V$ $\tau_m = 0.108\ ms$

(b) $V_m = 116.5\ V$ $\tau_m = 0.131\ ms$

(c) $V_m = 128.6\ V$ $\tau_m = 0.147\ ms$

Table 3 Energy balance

Energy in/energy out, kW	E_b, V/m		
	0.8×10^5	1×10^5	1.2×10^5, V/m
Total power dissipated through the joule heating	21.78	22.6	24.5
Total radiation out of the torch	6.17	6.4	7.1
Thermal conduction to the cathode (plasma)	0.33	0.33	0.33
Thermal conduction to the anode (plasma)	2.09	2.1	2.15
Cooling through the neutrode/converging nozzle surfaces	2.43	2.65	2.83
Energy out from the torch	7.79	8.4	9.57
Thermal efficiency	34%	37.1%	39%

at $z = 0.069$ mm (the start of the extended domain) and this value time-averaged over minimum ten restrike periods. The final value includes the radiation losses to the electrode walls, neutrode, converging nozzle walls and the exit.

Other heat losses from the plasma, including conduction heat losses to the electrodes and the neutrode/converging nozzle, are straightforward to calculate using the convective heat transfer coefficient. Finally, the main focus parameter, the exit power of the torch, is calculated by time-averaging the areal integration of the energy flux at the actual outlet of the domain ($z = 0.069$ mm).

In Table 3, it is evident that the total mean joule power of the torch increases as the E_b value rises. This increase can be attributed to the longer mean arc column length (also reflected in the arc voltage) for a particular E_b. Specifically, the corresponding values of joule power are 21.78 kW, 22.6 kW, and 24.5 kW for E_b values of 0.8×10^5 V/m, 1.0×10^5 V/m, and 1.2×10^5 V/m, respectively. In terms of energy losses, the majority of the plasma cooling occurs through radiation, accounting for nearly 28% of the joule heat dissipated in the torch in all cases. Similarly, the total radiation emitted depends on the mean arc length and thus the E_b value. The maximum radiation cooling observed is nearly 7.1 kW for an E_b value of 1.2×10^5 V/m, with other radiation losses recorded at 6.17 kW (0.8×10^5 V/m) and 6.4 kW (1×10^5 V/m). Conduction losses at solid surfaces, such as the cathode, anode, neutrode, and converging nozzle, contribute to the remaining heat losses. The lowest losses are observed at the cathode surface, nearly constant for all three E_b values, at approximately 0.33 kW. While the variation of joule heating with changing E_b has no influence on cathode heat losses, anode losses are approximately six times greater than cathode losses across all cases, averaging around 2.1 kW with minor variations among the considered E_b values. Heat losses from the neutrode/converging nozzle are significant, even exceeding those of the anode, with values of 2.43 kW, 2.65 kW, and 2.83 kW for E_b values of 0.8×10^5 V/m, 1×10^5 V/m, and 1.2×10^5 V/m, respectively. The variation in heat losses from the converging

nozzle with different values of E_b can be attributed to several specific traits of this section. Firstly, the nozzle is angled relative to the torch direction, causing the forced plasma jet to approach the converging section more closely. Secondly, the nozzle has a non-circular shape, which is thermally less efficient compared to circular designs. Finally, the diameter of this section decreases along its length, reducing to half of its initial value. These characteristics result in substantial heat losses that vary with different values of E_b, as the length of the high-temperature jet significantly affects the converging nozzle.

Finally, the energy released from the torch increases as the E_b value rises. The corresponding exit powers were 7.79 kW, 8.4 kW, and 9.57 kW, yielding thermal efficiencies of 34%, 37%, and 39%, respectively. The thermal efficiency of the torch was obtained by dividing the exit power of the torch with total joule heat dissipated in the torch. It is worth noting that the reported efficiencies do not account for the sheath voltage or power at the electrodes (13 V). When factoring in these elements, the predicted efficiencies would slightly decrease to 32%, 33%, and 35.3%, respectively. Therefore, the total power of the torch, after incorporating the voltage drops, should be 24.4 kW, 25.2 kW, and 27.1 kW.

The validation of the aforementioned case involving straight gas inlet was challenging to obtain. However, there were some experimental results conducted by SAFRAN under similar conditions but with the actual geometry involving the vortex generator (VG). The operating conditions were 200A and 100 SLPM with a mixture of Argon (80%) and Hydrogen (20%). It's worth noting that the experimental measurements were conducted for the entire Axial III plus setup, which includes the other two torches as well. Therefore, assuming that the behavior of the three torches was the same, the total power dissipated could be divided into three values, each totaling 27 kW, corresponding to a thermal efficiency of 32%.

It appears that the predicted values are reasonably close to the experimental measurements. At an E_b value of 1.2×10^5 V/m, the total power is nearly 27 kW for both

cases, with the predicted thermal efficiency being 3% higher. This discrepancy might be attributed among other to experimental conditions favoring higher mean arc lengths in straight gas flow compared to swirl flows. Additionally, the reported experimental voltage drops (136.2 V) are relatively close to the predicted voltage drop (128 V + sheath drop 13 V = 141 V). Due to the difficulty in measuring the voltage of individual cathodes in the Axial III Plus, the presented voltage drop is measured at the power supply point. This overall value accounts for all three torches and includes losses in the cables as well.

The simulation of the current model incorporating a vortex generator (VG) was beyond the scope of this study due to significant restrictions on Local Thermodynamic Equilibrium (LTE) conditions in swirl gases. Increased cooling of the arc column in such configurations enhances the non-equilibrium nature of the plasma, necessitating a non-LTE model (Ref 50). The inclusion of a VG has the potential to reduce voltage trace fluctuations, leading to a decrease in voltage jump amplitude and shorter arc spot lifetimes. Mohanty et al. reported jump amplitudes and arc spot lifetimes of approximately 65 V and 0.1 ms, respectively, for a 200A arc current using the 100HE torch (Ref 8). Similarly, Zimmermann et al.'s experimental measurements with the Axial III have shown comparable jump amplitudes and slightly lower arc spot lifetimes (0.087 ms), although their experiment was conducted at 230 A (Ref 12). It is important to note that both studies used higher flow rates than the present work, so the comparisons are not absolute. However, they support the idea that, even at higher gas flow rates, the lower jump amplitudes and the arc spot lifetimes may result from using a VG.

Both the Axial III guns and the 100HE torch typically utilize some amount of nitrogen along with argon and hydrogen to maximize the torch's exit enthalpy (Ref 51) and thermal conductivity (Ref 46), which are crucial for enhancing deposition efficiency in the SPS process. Simulation of the Axial III gun with a ternary gas mixture is limited due to the lack of thermodynamic and transport property data. It has been demonstrated that nitrogen plasmas increase arc constriction (arc current density) compared to argon plasmas (Ref 52). This increased constriction raises the electric field at the arc column fringes, thereby requiring lower threshold (E_b)) values for simulating the restrike mode. Furthermore, arc constriction implies that for a constant arc length, the nitrogen arc will exhibit a higher voltage drop compared to the argon arc. It is concluded that the addition of nitrogen to the argon–hydrogen mixture will have a significant impact on the arc structure, especially increasing its length, thereby affecting arc voltage, and significantly improving the thermal efficiency of the torch.

Conclusions

In this study, an LTE thermal plasma model, coupled with a restrike model, was employed to simulate the electric arc restrike behavior and flow fields within the novel torch utilized in the Axial III Plus system. The numerical model solved the MHD fluid equations, alongside the coupled solid transient heat diffusion equation, to characterize the fluid, thermal, and electromagnetic fields within the plasma and electrodes. However, these equations alone may not sufficiently capture the complex arc dynamics during restrike mode, necessitating the utilization of a restrike model based on threshold criteria for the mean radial electric field predicted at the electric arc fringes.

The following conclusions can be drawn from this study:

(1) The initial examination of predicted self-induced magnetic field profiles and electrode temperatures is crucial, as they influence the cold boundary layer thickness around the anode, subsequently impacting the mean radial electric field—the core parameter of the restrike model. The accurate prediction of the magnetic field is particularly significant given the complex torch design of the Axial III system, where the anode's inner diameter varies along its length. Temperature distributions across surfaces and bulk regions appear consistent and align with existing literature.

(2) Employing the restrike model, our results accurately replicate typical electric arc behavior during restrike mode, which is pertinent to the operation of the Axial III Plus plasma torch, characterized by low arc currents and high gas flow rates. Our findings reveal the influence of the special design of the anode nozzle surface on arc connection and voltage dynamics over time, with consequent effects on plasma temperature and velocity.

(3) Further analysis investigates the effect of varying the threshold radial electric field (E_b) on the restrike nature of the electric arc. Higher E_b values result in delayed artificial arc breakdown during the restrike process, leading to longer mean arc lengths and mean arc spot times. The rise in mean electric arc column length with increasing E_b can be attributed to increased joule heating and radiation losses in the torch's energy balance. While radiation accounts for a significant portion of losses, conduction heat losses at the cathode surface are minimal, nearly six times lower than those observed at the anode surface. E_b values do not significantly affect variations in conduction heat losses at the electrodes, although slightly higher variations in heat losses are observed

in the converging nozzle section, likely due to heat transfer variation associated with forced plasma jet through the converging nozzle section and non-circular shape converging nozzle boundary itself.

This study, conducted using the LTE model, provides insights into electric arc behavior during restrike mode in the specially designed arc plasma torch of the Axial III Plus setup. While the model does not incorporate the vortex generator (VG) and nitrogen gas commonly used in Axial III plasma torch operation, their potential impacts have been discussed referencing the works of Mohanty et al. (Ref 8) and Zimmermann et al. (Ref 12). These findings lay the groundwork for future simulations of Axial III torches, incorporating VG and ternary gas mixtures, to enhance our understanding and optimize torch performance.

For future modeling of this geometry, two crucial steps are necessary:

1. Inclusion of a Vortex Generator (VG):

   • Incorporating a VG at the inlet section, along with proper meshing, is essential to accurately capture the finer variations in velocity gradients. The VG significantly modifies the flow field, and including it in the model will provide more realistic simulations of the plasma torch operation.

2. Adopting a Two-Temperature Formulation:

   • The addition of a VG complicates the model by increasing the cooling effect, thus necessitating a two-temperature formulation to accurately capture the thermal behavior of the plasma and its interaction with the surrounding gases. This approach requires comprehensive thermodynamic and transport property data for dual and ternary gas mixtures. Such data is currently not readily available in the literature, especially at higher non-equilibrium degrees. Obtaining these data is crucial for developing more accurate and predictive models of plasma torches with vortex generators.

By addressing these steps, future simulations will better reflect the real-world performance of plasma torches, ultimately leading to more effective and efficient designs.

References

1. F.-L. Toma, A. Potthoff, L.-M. Berger and C. Leyens, Demands, Potentials, and Economic Aspects of Thermal Spraying with Suspensions: A Critical Review, *J. Therm. Spray Technol.*, 2015, **24**(7), p 1143-1152. https://doi.org/10.1007/s11666-015-0274-7

2. M.R. Dorfman, G. Dwivedi, C. Dambra and S. Wilson, Perspective: Challenges in the Aerospace Marketplace and Growth Opportunities for Thermal Spray, *J. Therm. Spray Technol.*, 2022, **31**(4), p 672-684. https://doi.org/10.1007/s11666-022-01351-x

3. H. Kassner, R. Siegert, D. Hathiramani, R. Vassen and D. Stoever, Application of Suspension Plasma Spraying (SPS) for Manufacture of Ceramic Coatings, *J. Therm. Spray Technol.*, 2008, **17**(1), p 115-123. https://doi.org/10.1007/s11666-007-9144-2

4. R.S. Lima, Porous APS YSZ TBC Manufactured at High Powder Feed Rate (100 g/Min) and Deposition Efficiency (70%): Microstructure, Bond Strength and Thermal Gradients, *J. Therm. Spray Technol.*, 2022, **31**(3), p 396-414. https://doi.org/10.1007/s11666-021-01302-y

5. Northwest Mettech Corp., "Axial III Spray System - Advanced Coating Solutions," n.d., https://www.mettech.com/assets/pdf/brochure_axail_III.pdf.

6. D. Zhou, O. Guillon and R. Vaßen, Development of YSZ Thermal Barrier Coatings Using Axial Suspension Plasma Spraying, *Coatings*, 2017, **7**(8), p 120.

7. S. Sampath, U. Schulz, M.O. Jarligo and S. Kuroda, Processing Science of Advanced Thermal-Barrier Systems, *MRS Bull.*, 2012, **37**(10), p 903-910. https://doi.org/10.1557/mrs.2012.233

8. P.S. Mohanty, A. George, L. Pollard and D. Snyder, A Novel Single Cathode Plasma Column Design for Process Stability and Long Component Life, *J. Therm. Spray Technol.*, 2010, **19**(1), p 448-458. https://doi.org/10.1007/s11666-009-9449-4

9. Z. Tang, H. Kim, I. Yaroslavski, G. Masindo, Z. Celler, and D. Ellsworth, Novel Thermal Barrier Coatings Produced by Axial Suspension Plasma Spray. pp. 571-575 (2011). https://doi.org/10.31399/asm.cp.itsc2011p0571.

10. D.A. Ross and A. Burgess, Plasma Jet Converging System (2005).

11. D.A. Ross and A. Burgess, Plasma Jet Converging System (1996).

12. S. Zimmermann, G. Mauer, K.-H. Rauwald and J. Schein, Characterization of an Axial-Injection Plasma Spray Torch, *J. Therm. Spray Technol.*, 2021, **30**(7), p 1724-1736. https://doi.org/10.1007/s11666-021-01235-6

13. N. Markocsan, M. Gupta, S. Joshi, P. Nylén, X.-H. Li and J. Wigren, Liquid Feedstock Plasma Spraying: An Emerging Process for Advanced Thermal Barrier Coatings, *J. Therm. Spray Technol.*, 2017, **26**(6), p 1104-1114. https://doi.org/10.1007/s11666-017-0555-4

14. S. Paik, P.C. Huang, J. Heberleinand and E. Pfender, Determination of the Arc-Root Position in a DC Plasma Torch, *Plasma Chem. Plasma Process.*, 1993, **13**(3), p 379-397. https://doi.org/10.1007/BF01465872

15. H.-P. Li, E. Pfender and X. Chen, Application of Steenbeck's Minimum Principle for Three-Dimensional Modelling of DC Arc Plasma Torches, *J. Phys. D Appl. Phys.*, 2003, **36**(9), p 1084. https://doi.org/10.1088/0022-3727/36/9/306

16. R. Huang, H. Fukanuma, Y. Uesugi and Y. Tanaka, Simulation of Arc Root Fluctuation in a DC Non-Transferred Plasma Torch with Three Dimensional Modeling, *J. Therm. Spray Technol.*, 2012, **21**(3), p 636-643. https://doi.org/10.1007/s11666-011-9710-5

17. B. Selvan, K. Ramachandran, K.P. Sreekumar, T.K. Thiyagarajan and P.V. Ananthapadmanabhan, Numerical and Experimental Studies on DC Plasma Spray Torch, *Vacuum*, 2009, **84**(4), p 444-452. https://doi.org/10.1016/j.vacuum.2009.09.009

18. E. Moreau, C. Chazelas, G. Mariaux and A. Vardelle, Modeling the Restrike Mode Operation of a DC Plasma Spray Torch, *J. Therm. Spray Technol.*, 2006, **15**(4), p 524-530. https://doi.org/10.1361/105996306X147306

19. R. Huang, H. Fukanuma, Y. Uesugi and Y. Tanaka, An Improved Local Thermal Equilibrium Model of DC Arc Plasma Torch, *IEEE Trans. Plasma Sci.*, 2011, **39**, p 1974-1982. https://doi.org/10.1109/TPS.2011.2163828

20. J.P. Trelles, J.V.R. Heberlein and E. Pfender, Non-Equilibrium Modelling of Arc Plasma Torches, *J. Phys. D Appl. Phys.*, 2007, **40**(19), p 5937. https://doi.org/10.1088/0022-3727/40/19/024

21. J.P. Trelles, E. Pfender and J. Heberlein, Multiscale Finite Element Modeling of Arc Dynamics in a DC Plasma Torch, *Plasma Chem. Plasma Process.*, 2006, **26**(6), p 557-575. https://doi.org/10.1007/s11090-006-9023-5

22. M. Alaya, C. Chazelas, G. Mariaux and A. Vardelle, Arc-Cathode Coupling in the Modeling of a Conventional DC Plasma Spray Torch, *J. Therm. Spray Technol.*, 2015, **24**(1), p 3-10. https://doi.org/10.1007/s11666-014-0162-6

23. M. Alaya, C. Chazelas and A. Vardelle, Parametric Study of Plasma Torch Operation Using a MHD Model Coupling the Arc and Electrodes, *J. Therm. Spray Technol.*, 2016, **25**(1), p 36-43. https://doi.org/10.1007/s11666-015-0330-3

24. R. Zhukovskii, C. Chazelas, V. Rat, A. Vardelle and R.J. Molz, Effect of Cathode-Plasma Coupling on Plasma Torch Operation Predicted by a 3D Two-Temperature Electric Arc Model, *J. Therm. Spray Technol.*, 2023, **32**(2), p 532-547. https://doi.org/10.1007/s11666-022-01501-1

25. W.Z. Wang, M.Z. Rong, J.D. Yan, A.B. Murphy and J.W. Spencer, Thermophysical Properties of Nitrogen Plasmas under Thermal Equilibrium and Non-Equilibrium Conditions, *Phys. Plasmas*, 2011, **18**(11), p 113502. https://doi.org/10.1063/1.3657426

26. V. Rat, P. André, J. Aubreton, M.F. Elchinger, P. Fauchais and A. Lefort, Transport Properties in a Two-Temperature Plasma: Theory and Application, *Phys. Rev. E*, 2001, **64**(2), p 026409. https://doi.org/10.1103/PhysRevE.64.026409

27. K.C. Meher, N. Tiwari and S. Ghorui, Thermodynamic and Transport Properties of Nitrogen Plasma Under Thermal Equilibrium and Non-Equilibrium Conditions, *Plasma Chem. Plasma Process.*, 2015, **35**(4), p 605-637. https://doi.org/10.1007/s11090-015-9615-z

28. J. Aubreton, M.F. Elchinger, P. Fauchais, V. Rat and P. André, Thermodynamic and Transport Properties of a Ternary Ar-H2-He Mixture out of Equilibrium up to 30 000 K at Atmospheric Pressure, *J. Phys. D Appl. Phys.*, 2004, **37**(16), p 2232. https://doi.org/10.1088/0022-3727/37/16/004

29. R. Zhukovskii, C. Chazelas, V. Rat, A. Vardelle and R. Molz, Predicted Anode Arc Attachment by LTE (Local Thermodynamic Equilibrium) and 2-T (Two-Temperature) Arc Models in a Cascaded-Anode DC Plasma Spray Torch, *J. Therm. Spray Technol.*, 2022, **31**(1), p 28-45. https://doi.org/10.1007/s11666-021-01253-4

30. P. Liang and R. Groll, Numerical Study of Plasma-Electrode Interaction During Arc Discharge in a DC Plasma Torch, *IEEE Trans. Plasma Sci.*, 2018, **46**(2), p 363-372.

31. S.A. Wutzke, E. Pfender and E.R.G. Eckert, Study of Electric Arc Behavior with Superimposed Flow, *AIAA J.*, 1967, **5**(4), p 707-713. https://doi.org/10.2514/3.4051

32. E. Eckert, E. Pfender, and S. Wutzke, Symptomatic Behavior of an Electric Arc with a Superimposed Flow. in *6th Electric Propulsion and Plasmadynamics Conference*, American Institute

33. G. Yang, P. Cronin, J.V. Heberlein and E. Pfender, Experimental Investigations of the Anode Boundary Layer in High Intensity Arcs with Cross Flow, *J. Phys. D Appl. Phys.*, 2006, **39**(13), p 2764. https://doi.org/10.1088/0022-3727/39/13/020

34. L. Prevosto, H. Kelly, B. Mancinelli and J.C. Chamorro, On the Gas Heating Mechanism for the Fast Anode Arc Reattachment in a Non-Transferred Arc Plasma Torch Operating with Nitrogen Gas in the Restrike Mode, *Plasma Chem. Plasma Process.*, 2015, **35**(6), p 1057-1070. https://doi.org/10.1007/s11090-015-9644-7

35. V. Nemchinsky, On Conductivity of Cold Gas Layer Separating Arc Column and Nozzle in Nontransferred Plasma Arc (Anode Reattachment Process in Plasma Spray Systems), *IEEE Trans. Plasma Sci.*, 2015, **43**, p 1-1.

36. J.P. Trelles, E. Pfender and J.V.R. Heberlein, Modelling of the Arc Reattachment Process in Plasma Torches, *J. Phys. D Appl. Phys.*, 2007, **40**(18), p 5635. https://doi.org/10.1088/0022-3727/40/18/019

37. Y. Cressault, M.E. Rouffet, A. Gleizes and E. Meillot, Net Emission of Ar-H2-He Thermal Plasmas at Atmospheric Pressure, *J. Phys. D Appl. Phys.*, 2010, **43**(33), p 335204. https://doi.org/10.1088/0022-3727/43/33/335204

38. R. Zhukovskii, C. Chazelas, A. Vardelle and V. Rat, Control of the Arc Motion in DC Plasma Spray Torch with a Cascaded Anode, *J. Therm. Spray Technol.*, 2020, **29**(1), p 3-12. https://doi.org/10.1007/s11666-019-00969-8

39. R. Zhukovskii, C. Chazelas, A. Vardelle, V. Rat and B. Distler, Effect of Electromagnetic Boundary Conditions on Reliability of Plasma Torch Models, *J. Therm. Spray Technol.*, 2020, **29**(5), p 894-907. https://doi.org/10.1007/s11666-020-01052-3

40. R. Zhukovskii, Towards a Reliable Numerical Model of DC Plasma Spray Torch Operation, (Institute of Research on Ceramics (IRCER)—UMR CNRS 7315), Université de Limoges (2020).

41. K. Shao, Y.-H. Hu, X. Meng, H.-J. Huang, S.-R. Sun and H.-X. Wang, Experimental Study on the Restrike Mode of a DC Arc Anode Attachment, *Plasma Chem. Plasma Process.*, 2021, **41**(5), p 1517-1534. https://doi.org/10.1007/s11090-021-10196-1

42. V. Rat and J.F. Coudert, A Simplified Analytical Model for DC Plasma Spray Torch: Influence of Gas Properties and Experimental Conditions, *J. Phys. D Appl. Phys.*, 2006, **39**(22), p 4799. https://doi.org/10.1088/0022-3727/39/22/010

43. J. Coudert, C. Chazelas, D. Rigot and V. Rat, From Transferred Arc to Plasma Torches, *High Temp. Mater. Process. Int. Q. High-Technol. Plasma Process.*, 2005, **9**, p 173-194.

44. A. Murphy, Transport Coefficients of Hydrogen and Argon-Hydrogen Plasmas, *Plasma Chem. Plasma Process.*, 2000, **20**, p 279-297.

45. A. Murphy, Transport Coefficients of Air, Argon-Air, Nitrogen-Air, and Oxygen-Air Plasmas, *Plasma Chem. Plasma Process.*, 1995, **15**, p 279–305.

46. A.B. Murphy and C.J. Arundell, Transport Coefficients of Argon, Nitrogen, Oxygen, Argon-Nitrogen, and Argon-Oxygen Plasmas, *Plasma Chem. Plasma Process.*, 1994, **14**(4), p 451-490. https://doi.org/10.1007/BF01570207

47. B. Sourd, J. Aubreton, M.E. Elchinger, M. Labrot and U. Michon, High Temperature Transport Coefficients in e/C/H/N/O Mixtures, *J. Phys. D Appl. Phys.*, 2006, **39**, p 1105-1119.

48. J. Perambadur, P. Shukla, A.Y. Klimenko, A.B. Murphy and V. Rudolph, Arc Dynamics in a Vortex-Stabilized Non-Transferred Plasma Torch with a Tangential Gas Feed, *J. Phys. D Appl. Phys.*, 2021, **54**(49), p 495501. https://doi.org/10.1088/1361-6463/ac2039

49. J. Perambadur, A.Y. Klimenko, V. Rudolph and P. Shukla, Investigation of Plasma Swirl Dynamics and Effects of

of Aeronautics and Astronautics (1967). https://doi.org/10.2514/6.1967-675

Secondary Gas Injection in a Vortex Gas Stabilized DC Arc Plasma, *Int. J. Heat Fluid Flow*, 2022, **95**, p 108978. https://doi.org/10.1016/j.ijheatfluidflow.2022.108978

50. M. Baeva and D. Uhrlandt, Non-Equilibrium Simulation of the Spatial and Temporal Behavior of a Magnetically Rotating Arc in Argon, *Plasma Sources Sci. Technol.*, 2011, **20**(3), p 035008. https://doi.org/10.1088/0963-0252/20/3/035008

51. G. Mor and V. Belashchenko, High Stability, High Enthalpy APS Process Based on Combined Wall and Gas Stabilizations of Plasma (Part 1: Process and Coatings Introduction), pp. 437-444 (2015). https://doi.org/10.31399/asm.cp.itsc2015p0437.

52. A. El-Zein, M. Talaat, G. El-Aragi and A. El-Amawy, Electrical Characteristics of Nonthermal Gliding Arc Discharge Reactor in Argon and Nitrogen Gases, *IEEE Trans. Plasma Sci.*, 2016, **44**(7), p 1155-1159.